



Cite this: *Phys. Chem. Chem. Phys.*,  
2016, **18**, 12860

# Diffusion of macromolecules in a polymer hydrogel: from microscopic to macroscopic scales†

D. Sandrin,<sup>‡a</sup> D. Wagner,<sup>‡b</sup> C. E. Sitta,<sup>‡c</sup> R. Thoma,<sup>d</sup> S. Felekyan,<sup>a</sup> H. E. Hermes,<sup>b</sup> C. Janiak,<sup>d</sup> N. de Sousa Amadeu,<sup>d</sup> R. Kühnemuth,<sup>\*a</sup> H. Löwen,<sup>\*c</sup> S. U. Egelhaaf<sup>\*b</sup> and C. A. M. Seidel<sup>\*a</sup>

To gain insight into the fundamental processes determining the motion of macromolecules in polymeric matrices, the dynamical hindrance of polymeric dextran molecules diffusing as probe through a polyacrylamide hydrogel is systematically explored. Three complementary experimental methods combined with Brownian dynamics simulations are used to study a broad range of dextran molecular weights and salt concentrations. While multi-parameter fluorescence image spectroscopy (MFIS) is applied to investigate the local diffusion of single molecules on a microscopic length scale inside the hydrogel, a macroscopic transmission imaging (MTI) fluorescence technique and nuclear magnetic resonance (NMR) are used to study the collective motion of dextrans on the macroscopic scale. These fundamentally different experimental methods, probing different length scales of the system, yield long-time diffusion coefficients for the dextran molecules which agree quantitatively. The measured diffusion coefficients decay markedly with increasing molecular weight of the dextran and fall onto a master curve. The observed trends of the hindrance factors are consistent with Brownian dynamics simulations. The simulations also allow us to estimate the mean pore size for the herein investigated experimental conditions. In addition to the diffusing molecules, MFIS detects temporarily trapped molecules inside the matrix with diffusion times above 10 ms, which is also confirmed by anisotropy analysis. The fraction of bound molecules depends on the ionic strength of the solution and the charge of the dye. Using fluorescence intensity analysis, also MTI confirms the observation of the interaction of dextrans with the hydrogel. Moreover, pixelwise analysis permits to show significant heterogeneity of the gel on the microscopic scale.

Received 16th December 2015,  
Accepted 17th March 2016

DOI: 10.1039/c5cp07781h

www.rsc.org/pccp

## 1. Introduction

The motion of macromolecules through disordered matrices is of great importance in analytical and preparatory techniques (chromatography,<sup>1</sup> expansion microscopy,<sup>2</sup> genomics,<sup>3</sup> biofilms<sup>4</sup>) as well as in biomedical (imbibition,<sup>5</sup> controlled drug delivery,<sup>6–9</sup> flow control,<sup>10</sup> implantable devices,<sup>9</sup> contact lenses,<sup>11</sup> cellular and

tissue engineering<sup>12,13</sup>) and technical applications (enhanced oil recovery<sup>14,15</sup>). From a fundamental point of view, precise measurements for model systems are needed to reveal the underlying transport principles.<sup>16–19</sup> It is known that the presence of obstacles slows down the transport and that this is more pronounced for larger molecules. However, the basic underlying mechanisms and their effects are not yet completely understood. In particular, the motion of particles through a gel matrix represents an intricate problem as the gel matrix can respond to the particle motion. A nontrivial dependence of the diffusion behavior on both the host and the guest, *i.e.* the gel and the diffusing particles, is expected. The behavior of the host is mainly characterized by a typical pore size. However, topological constraints resulting from the nontrivial and dynamically changing connectivity of the pores<sup>20</sup> also have an impact on the diffusion of the guest molecules. This connectivity is expected to result in a wide spread in the translocation rate of the individual particles. The translational rate is also influenced by the structural properties of the guest molecules

<sup>a</sup> Institut für Physikalische Chemie II, Molekulare Physikalische Chemie, Heinrich-Heine-Universität, Universitätsstr. 1, 40225 Düsseldorf, Germany. E-mail: ralf.kuehnemuth@hhu.de, cseidel@hhu.de

<sup>b</sup> Institut für Experimentelle Physik der Kondensierten Materie, Heinrich-Heine-Universität, Universitätsstr. 1, 40225 Düsseldorf, Germany. E-mail: stefan.egelhaaf@hhu.de

<sup>c</sup> Institut für Theoretische Physik II: Weiche Materie, Heinrich-Heine-Universität, Universitätsstr. 1, 40225 Düsseldorf, Germany. E-mail: hlowen@hhu.de

<sup>d</sup> Institut für Anorganische Chemie und Strukturchemie, Heinrich-Heine-Universität, Universitätsstr. 1, 40225 Düsseldorf, Germany

† Electronic supplementary information (ESI) available. See DOI: 10.1039/c5cp07781h

‡ These authors have contributed equally to this work.

such as hydrodynamic radius, shape, molecular weight or charge distribution. The significance of sieving, entanglements, (chemical) interactions, partitioning, oscillation of pores *etc.* is still controversially discussed.<sup>21–27</sup> In addition, the average size of the pores is also under debate.<sup>23,28–34</sup>

It is accepted that the mesh sizes in polymer hydrogels depend on the specific gel preparation such as (I) the mass concentration of polymeric material in the reaction solution,  $[T]$ , and (II) the weight fraction of cross-linker,  $C_R$ , but the absolute average size of the pores is subject to debate.<sup>23,28–34</sup> Considering hydrogels ( $0.035 \text{ g ml}^{-1} \leq [T] \leq 0.065 \text{ g ml}^{-1}$ ,  $0.02 \leq C_R \leq 0.05$ ) with similar compositions to the one studied here ( $[T] = 0.04 \text{ g ml}^{-1}$ ,  $C_R = 0.035$ ), different methods give very different results for the pore sizes (please note that the numbers given for  $[T]$  and  $C_R$ , multiplied by 100, correspond to the parameters %T and %C, respectively, which were used in the above publications). The reported pore sizes range from 2.00–2.25 nm (chromatography<sup>28</sup>) through 5–9 nm (electrophoresis studies in the 1960s and 1980s<sup>29,30</sup>) and 60–156 nm (electrophoresis studies in 1991<sup>23,31</sup>) up to values of 2–20  $\mu\text{m}$  (for the largest pores found by scanning electron microscopy<sup>32–34</sup>). This also complicates any systematic study of particle diffusion in a well-characterized model system, which however is important to understand the principles of translocation and to test theoretical approaches.

Here we study polymeric dextran molecules diffusing through a polyacrylamide hydrogel without interfering with the sample during the measurements. We use dextrans as tracer particles, because they have a good water solubility, low toxicity, relative inertness and are flexible polymers. Moreover, they are commercially available over a broad range of molecular weights and hence sizes. Most dextrans can be also obtained as derivatives labelled with fluorescent dyes (fluorescein sodium salt (FLU), Alexa Fluor 488 (A488), tetramethylrhodamine (TMR)). The molecular weight of the dextrans is varied between  $M_w = 3 \text{ kDa}$  to 2000 kDa. For comparison the diffusion of free dyes, FLU, A488 and TMR is studied in our hydrogel, too. To investigate the interactions of the particles with the hydrogel in more detail, we study the influence of solution conditions like pH-value, salt and tracer particle concentrations. Using three complementary methods, multiparameter fluorescence image spectroscopy (MFIS), macroscopic transmission imaging (MTI) with fluorescence detection and nuclear magnetic resonance (NMR), we measure the long-time diffusion coefficient of the fluorescently labelled and unlabelled probe particles, respectively. MFIS also allows us to detect the heterogeneity of the gel. The data are compared to a model by Ogston<sup>35</sup> which predicts the dynamical hindrance in a network of randomly distributed fibers due to geometric confinement. The Ogston model provides a simple analytical formula for the particle dynamics *via* an effective excluded volume. Another theoretical approach is to perform computer simulations. As modeling a hydrogel on an atomic basis over huge length- and timescales is computational unaffordable, various different model assumptions including different degrees of molecular details have been used in the past.<sup>36–48</sup> The most detailed model for the gel matrix was used by Linse and

coworkers<sup>36–39</sup> and Holm and coworkers<sup>40–42</sup> who resolved the monomers of the polymer chains connecting the nodes explicitly within a bead-spring model. Within their approach the swelling behavior of the gels was explored but the diffusion of tracer particles within the gel network was not addressed. In a more coarse-grained approach, the matrix was described by either a static network of points,<sup>43</sup> rods,<sup>43,44</sup> or chains<sup>45</sup> or as fluctuating network of spheres<sup>46,47</sup> which indeed allows for the computation of tracer diffusion. Following the latter coarse grained approach of Zhou and Chen,<sup>47</sup> we perform Brownian dynamics (BD) simulations representing three different levels of complexity to resolve the different physical effects that are operating in the hydrogel. Our simulation study provides a simple and systematic framework, taking into account the flexibility of the matrix particles, the effective dextran–matrix excluded volume and finding strong indications for effective attractive interactions. Our combined results provide a consistent picture of polymers diffusing through a hydrogel matrix and may serve to test more quantitative theories and other experimental approaches.

## 2. Materials and methods

### 2.1. Samples

**2.1.1. Hydrogel: a polymer matrix in an aqueous environment.** The polyacrylamide (PAAm) hydrogels were formed by copolymerization of acrylamide (AAM, monomer) with the tetrafunctional cross-linking agent *N,N'*-methylenebis(acrylamide) (BIS), using ammonium peroxodisulphate (APDS) and tetramethylethylenediamine (TEMED) as redox initiators. The monomer and cross-linker were both purchased from Sigma-Aldrich, APDS from Roth and TEMED from Merck. All components were used without further purification. AAM, BIS and APDS were separately dissolved in deionized and filtered water and cooled to 4 °C. The individual solutions were then mixed at a low temperature. The reaction mixture contained 75 mg of AAM, 2.71 mg of BIS, 6 mg of APDS and 10  $\mu\text{l}$  of TEMED in a total volume of 2 ml which corresponds to a molar ratio of cross-linker to monomer of 1:60. The total monomer concentration, defined as the mass concentration of AAM and BIS in the total reaction volume, is  $[T] = 0.04 \text{ g ml}^{-1}$  and the weight fraction of cross-linker with respect to the total mass of the polymeric material (AAM and BIS) is  $C_R = 0.035$ .

After mixing, the solution was transferred to Teflon molds and allowed to warm up and react at room temperature. After one to two hours, polymerization was complete and the hydrogel was transferred into a larger container filled with deionized water. The gel was left for five days to ensure that the hydrogel swells to equilibrium. The excess water was exchanged daily to wash out residual chemicals that had not reacted in the gelation process.<sup>49</sup>

Discs with a radius  $R_d \approx 0.3 \text{ cm}$  were cut from the hydrogels using a simple stamp. In corresponding MTI and MFIS experiments, samples cut from one gel block were used. For the NMR measurements, the gelation process was carried out in cylindrical

Teflon molds ( $R_d \approx 0.5$  cm, height 5 cm). The hydrogels were then transferred into a container filled with deuterium oxide.

The hydrogel was characterized by determining the polymer volume fraction in the fully swollen state,  $\phi$ , the average molecular weight between cross-linking points,  $M_c$ , and the mesh size,  $\xi$ . The polymer volume fraction of the hydrogel in the swollen state  $\phi$  was calculated directly from eqn (1):<sup>50,51</sup>

$$\phi = \frac{V_p}{V_{\text{gel}}} = \frac{m_p \rho_{\text{H}_2\text{O}}}{m_p \rho_{\text{H}_2\text{O}} + m_{\text{H}_2\text{O}} \rho_p} \quad (1)$$

where  $V_p$  is the volume of the dry polymer (PAAm),  $V_{\text{gel}}$  is the volume of the hydrogel after equilibrium swelling,  $m_p$  is the mass of the polymer,  $m_{\text{H}_2\text{O}}$  is the mass of water in the swollen gel and  $\rho_p$  and  $\rho_{\text{H}_2\text{O}}$  are the densities of polymer and water, respectively.

The mass of the fully swollen hydrogel was measured after removing the liquid on the surface of the hydrogel with a pipette. It was then dried at 40 °C under vacuum for at least 6 h until constant weight was reached to determine  $m_p$ . The experiment was repeated for different pieces of hydrogel, and the mass fraction was converted into volume fraction using the known polymer density ( $\rho_p = 1.3$  g cm<sup>-3</sup>).<sup>52</sup>

The theoretical molecular weight of the polymer between cross-links  $M_c$  is related to the degree of cross-linking in the hydrogel,  $X$  (*i.e.*, the molar ratio of cross-linker to monomer) and the molecular weight of the repeating units ( $M_{r,\text{AAm}} = 71.1$  g mol<sup>-1</sup>):<sup>51,53</sup>

$$M_c = \frac{M_r}{2X} \quad (2)$$

The mesh size,  $\xi$ , which characterizes the space between macromolecular chains can be calculated using:<sup>50,54,55</sup>

$$\xi = \phi^{-1/3} \zeta \left( \frac{C_n 2M_c}{M_r} \right)^{1/2} \quad (3)$$

where  $C_n$  is Flory's characteristic ratio ( $C_{n,\text{AAm}} = 2.72$ ) and  $\zeta$  is the carbon-carbon bond length ( $\zeta = 0.154$  nm).<sup>56</sup> This calculation assumes ideal solvent quality, homogeneous cross-linking densities and Gaussian distribution of chain lengths.

We characterized the polyacrylamide hydrogels as used in these experiments, *i.e.* in water and in a 20 mM potassium carbonate buffer at pH 10. The results are shown in Table 1.

**2.1.2. Diffusing polymeric guest molecules.** The dextrans (Table 2) and free dyes were purchased from Invitrogen. For the NMR experiments, unlabelled dextrans were dissolved in deuterium oxide with a purity of 99.9% from Deutero GmbH. For the remaining experiments, dextrans conjugated with Alexa

**Table 2** Overview of dyes and dextrans of different molecular weights,  $M_w$ , as obtained from manufacturer (for labelled dextrans already including the dye) and their naming convention. The dextrans were either unlabelled or conjugated with one of three different dyes: Alexa Fluor 488, tetramethylrhodamine and fluorescein. For more detailed information see S1.1 and S1.2 (ESI)

| $M_w$<br>[kDa] | Unlabelled | Alexa<br>fluor 488 | Tetramethylrhodamine | Fluorescein |
|----------------|------------|--------------------|----------------------|-------------|
| 0.33           |            |                    |                      | FLU         |
| 0.39           |            |                    | TMR                  |             |
| 0.53           |            | A488               |                      |             |
| 3              | D3         | A488-D3            | TMR-D3               | FLU-D3      |
| 10             | D10        | A488-D10           | TMR-D10              | FLU-D10     |
| 40             | D40        |                    | TMR-D40              | FLU-D40     |
| 70             |            |                    | TMR-D70              |             |
| 500            |            |                    |                      | FLU-D500    |
| 2000           |            |                    | TMR-D2000            |             |

Fluor 488 (A488) or tetramethylrhodamine (TMR) were dissolved in deionized water. To exclude fluorescence blinking due to protonation-deprotonation dynamics, dextrans labelled with fluorescein (FLU) were prepared in potassium carbonate buffer at pH = 10, (20 mM) and the fluorescence measurements were conducted after addition of 100  $\mu$ M Trolox (Sigma-Aldrich) to avoid photobleaching of the dye.

To investigate the local environment and possible probe-polymer interactions inside the gel matrix, we measured the most polar dye attached to one of the smaller dextrans, A488-D10 under five different conditions: (i) H<sub>2</sub>O, (ii) aqueous KClO<sub>4</sub> solution (10 mM, 20 mM, 40 mM, and 60 mM), (iii) aqueous KCl solution (20 mM), (iv) aqueous potassium carbonate buffer (20 mM) at pH = 7, and (v) at pH = 10.

**2.1.3. Addition of polymeric guest molecules to the hydrogel.** For MFIS experiments, each hydrogel disc was placed in a chambered cover glass (Lab-Tek™, Thermo Fisher Scientific, USA), incubated with guest molecule solution (400  $\mu$ l in total) and allowed to reach equilibrium before the measurement was started (2 to 7 days depending on dextran size). When electrolyte solutions were used, the solution was exchanged approximately every 12 h during the incubation period to ensure defined concentrations.

In the MTI experiments, the initial particle concentration in the hydrogel was 0 and the concentration in the surrounding solution was varied between 0.1 and 10  $\mu$ M. The hydrogel matrix was contacted with the particle (dye or dextran) solution at the beginning of the experiments and the diffusion of guest molecules from the solution into the hydrogel was studied.

For NMR measurements, the hydrogel cylinders were incubated with concentrated amino dextran solution in deuterium oxide for at least 48 h. The samples were then carefully transferred into NMR tubes ensuring that the gel texture was not destroyed. Concentrations below 1 mM were used in order to avoid aggregation. Bubbles were successfully avoided.

## 2.2. Measurement methods

**2.2.1. Multiparameter fluorescence image spectroscopy (MFIS).** All measurements were conducted on a confocal fluorescence microscope (FV1000 Olympus, Hamburg, Germany),

**Table 1** Polymer volume fraction in the swollen state ( $\phi$ ), molecular weight of the polymer between cross-links ( $M_c$ ) and mesh size ( $\xi$ ) for the PAAm hydrogel in water and in potassium carbonate buffer 20 mM at pH 10. The errors are the standard errors of repeated measurements of the polymer volume fraction

|                              | PAAm in water       | PAAm pH 10          |
|------------------------------|---------------------|---------------------|
| $\phi$                       | 0.0390 $\pm$ 0.0004 | 0.0150 $\pm$ 0.0001 |
| $M_c$ [g mol <sup>-1</sup> ] | 2141                | 2141                |
| $\xi$ [nm]                   | 5.7 $\pm$ 0.1       | 7.8 $\pm$ 0.1       |

which had been modified to allow time-resolved experiments.<sup>57,58</sup> A488 and FLU were excited using a polarized pulsed diode-laser (LDH-D-C-485, PicoQuant, Berlin, Germany) at 485 nm, while for TMR a supercontinuum laser (SuperK Extreme, NKT Photonics, Birkerød, Denmark) at 555 nm was employed. Laser light was directed into a 60× water immersion objective (NA = 1.2) by a dichroic beam splitter and focused into the sample close to the diffraction limit. The light emitted was collected by the same objective and separated into two polarizations (parallel and perpendicular) relative to the excitation beam. The fluorescence signal was further divided into two spectral ranges (BS 560, AHF, Tübingen, Germany). Bandpass filters for A488/FLU and TMR fluorescence (HC 520/35 and HC 607/70, AHF), were placed in front of the detectors. The signal from single photon sensitive detectors (PDM50-CTC, Micro Photon Devices, Bolzano, Italy and HPMC-100-40, Becker&Hickl, Berlin, Germany, respectively) was recorded photon-by-photon with picosecond accuracy (HydraHarp400, PicoQuant) and analyzed using custom software (LabVIEW based). The temperature during all measurements was  $22.5 \pm 0.5$  °C and the concentration of the dextrans was adjusted between 0.05 and 3 nM, depending on their different degree of labelling.

The sample was mounted on a piezo-controlled x-y scanner (P-733.2CL, Physik Instrumente, Karlsruhe, Germany) and moved perpendicular to the optical axis. It was moved in a stepwise manner to permit multiparameter fluorescence detection at defined locations. The pixel size is defined by the step size of the scan (in our experiments 10.00 μm) while photons are collected from the confocal detection volume only ( $V_{\text{det}} = 0.55$  fl). The integration time per pixel was 30 min and the complete image contains 18 pixels (probed spots).

**2.2.2. Macroscopic transmission imaging (MTI).** The macroscopic transmission imaging experiments were performed using a custom-built imaging apparatus similar to that described previously.<sup>59</sup> The sample was illuminated by a parallel beam of light from an LED lamp (CoolLED, center wavelength of 490 nm) whose wavelength was chosen to excite the fluorescent particles in the sample. Using a dichroic mirror that transmits wavelengths above and reflects wavelengths below 502 nm, the transmitted light was split into excitation light (bright-field transmission image) and emitted light from the fluorophores (fluorescence image). The images were then focused onto separate CCD cameras. Additional fluorescence filters (excitation filter: 480/25, emission filter: longpass LP 520) were applied. The hydrogel discs were placed between two horizontally held glass plates with a fixed distance between the plates of 1.5 mm using aluminum spacers. This distance was chosen to ensure that the gels were compressed as little as possible but still in contact with both glass plates. The particle solution was added around the gel discs and allowed to diffuse into the gel matrix. The image collection time was varied between 5 s at the beginning and up to 300 s at the end of a measurement. Images were collected for 3 to 72 h. The sample cells were sealed to ensure that the solvent did not evaporate and measurements were performed at room temperature (23 °C).

**2.2.3. Nuclear magnetic resonance (NMR).** A Bruker AVANCE DRX-500 NMR spectrometer operating at 500 MHz for <sup>1</sup>H was used. The spectrometer was equipped with a Bruker Great 1/10 gradient amplifier and a Bruker selective inverse (SEI) probe with z-gradient coils. The gradient amplitudes were calibrated using dodecane, 1-pentanol and water as standard samples.<sup>60</sup> The temperature sensor was calibrated using methanol as described by van Geet.<sup>61</sup> All diffusion measurements were acquired by using stimulated echo with bipolar gradient pulses (pulse program name STEBPGP).<sup>62,63</sup> This sequence was also followed by a WATERGATE sequence to suppress the water signal.<sup>64,65</sup>

In each experiment, the magnetic field gradient strength of the bipolar pulses was linearly arrayed along 16 values from 10 to 60 G cm<sup>-1</sup> while all other parameters were kept constant. The gradient pulse length,  $\delta$  and the diffusion delay,  $\Delta_N$ , were chosen such that the echo signal was suppressed considerably.

The diffusion coefficients of unlabelled aminodextrans in hydrogels and in deuterium oxide were measured at 23 °C in NMR sample tubes of 5 mm diameter. Dextran concentrations depended on the dextran's molecular weight and varied from 3.0 M for the 3 kDa dextran to 0.3 M for the 40 kDa dextran to avoid agglomeration in solution. We performed several diffusion measurements with each sample, varying the key parameters  $\delta$  and  $\Delta_N$ . Our experience showed that this is a good practice which helps identifying artifacts affecting the experiments or errors in the processing routines. The diffusion delays,  $\Delta_N$  were chosen between 0.1 and 2.0 s and the gradient pulse widths,  $\delta$  were between 600 and 1400 μs. Several combinations of  $\Delta_N$  and  $\delta$  were applied within those ranges. Later examination revealed high agreement among all those measurements, indicating good reproducibility.

## 2.3. Analysis methods

**2.3.1. Multiparameter fluorescence image spectroscopy (MFIS).** The recorded MFIS data can be correlated to yield correlation curves (fluorescence correlation spectroscopy, FCS, is part of the MFIS). Those fluorescence correlation curves that were measured inside the hydrogel usually exhibited multiple overlapping bunching terms in the time regime of the diffusion process. To establish the number of independent species,  $M$ , needed in the model function to reproduce the data, we fitted a distribution of diffusion coefficients applying the maximum entropy method (MEMFCS).<sup>66</sup> Having determined  $M$  we then fitted a model function containing  $M$  diffusion terms (eqn (4)):

$$G(t_c) = 1 + \frac{1}{N} \sum_{i=1}^M x_i \left( \left( 1 + \frac{t_c}{t_{d,i}} \right) \sqrt{1 + \frac{t_c}{(z_0/\omega_0)^2 \cdot t_{d,i}}} \right)^{-1} \times \left( 1 - A_T + A_T \cdot e^{-\frac{t_c}{\tau}} \right) \quad \text{with} \quad \sum_{i=1}^M x_i = 1 \quad (4)$$

For species with identical brightness,  $x_i$  represents their true molecular fractions. In this case,  $N$  is the number of molecules in the singlet state in the detection volume element and  $t_c$  is the correlation time. The model assumes a three-dimensional Gaussian-shaped volume element with spatial distribution of

the detection probabilities  $w(x,y,z) = \exp(-2(x^2 + y^2)/\omega_0^2) \exp(-2z^2/z_0^2)$ . The  $1/e^2$  radii in  $x$  and  $y$  or in  $z$  direction are denoted by  $\omega_0$  or  $z_0$ , respectively. The characteristic diffusion time is  $t_d = \omega_0^2/4D$ , with the translational diffusion coefficient  $D$ . The confocal detection volume,  $V_{\text{det}}$  is calculated as follows:  $V_{\text{det}} = \pi^{3/2}z_0\omega_0^2$ .

Basic photophysical processes such as triplet transitions which result in temporary dark states are accounted for by an additional bunching term. Here  $A_T$  and  $t_T$  represent the triplet population and the triplet relaxation time.

The correlation curves for A488- and TMR-dextran in water and most FLU-dextran in carbonate buffer were fitted pixel by pixel, the remaining samples image-integrated. At mean irradiances in the focus of  $1.2 \text{ kW cm}^{-2}$ , A488- and TMR-samples did not exhibit noticeable triplet populations ( $A_T < 0.01$ ), only fluorescein showed fluorescence bunching in the  $\mu\text{s}$  regime at even lower irradiances of  $0.4 \text{ kW cm}^{-2}$ . For pixelwise analysis, error bars for  $t_d$  (and equivalently for  $D$ ) were calculated as standard error of the mean while for single point (*i.e.* solution) or image integrated measurements a bootstrapping procedure was applied.

Diffusion coefficients can be derived from the extracted diffusion times ( $t_d$ ) provided that the size and shape of the confocal detection volume element are characterized. In practice, a photostable reference dye with known diffusion properties is used to calibrate the system. In the present case, we chose rhodamine 110 (Rh110). Thus all presented diffusion coefficients derived from FCS are based on the reported value of  $D_{\text{Rh110}} = (4.3 \pm 0.3) \times 10^{-6} \text{ cm}^2 \text{ s}^{-1}$  at 295.65 K in dilute aqueous solutions.<sup>67</sup> The characteristic diffusion time of Rh110 in deionized water was  $t_d = 30 \mu\text{s}$  with day-to-day variations of less than 5%. Due to increased aberrations with changes in the refractive index upon addition of salt, a systematic increase of  $t_d$  was observed (*e.g.*  $t_d = 33 \mu\text{s}$  for Rh110 in 20 mM potassium carbonate buffer at pH 7 and pH 10, respectively). The longer wavelength required for the TMR experiments caused an increase in focus area  $\pi\omega_0^2 = t_d 4\pi D$  and thus of  $t_d$  of about 30%, as expected from the changed diffraction limit.

A variety of possible artifacts have been reported that could cause uncertainties in translational diffusion measurements by FCS.<sup>68</sup> In particular optical saturation effects are known to distort the detection volume element and thus alter the observed average dwell times of the fluorophores. These effects have been minimized by keeping the excitation power low and by performing reference measurements under identical conditions. Low excitation power also diminishes the probability of photobleaching. Successful minimization of this effect is confirmed by the observation of extremely slow diffusing molecules with dwell times of up to 1 s.

A further possible artifact, focal distortions due to a refractive index mismatch (below 0.01, see S1.6, ESI†) is estimated to result in a small corresponding error in  $D$  (below 1%<sup>69</sup>). This is supported by the good agreement of the FCS data with the independent MTI and NMR results (see below). Additionally, the possible refractive index mismatch between solution and hydrogel was checked using FCS and found to be negligible.

No readjustment of the correction collar setting on the objective was required after switching the sample from pure water to hydrogel (see S1.6, ESI†).

The steady state anisotropy,  $r$ , which is another parameter detected by MFIS is defined *via* the intensities of the fluorescence signal polarized parallel ( $F_{\parallel}$ ) and perpendicular ( $F_{\perp}$ ) with respect to the excitation polarization. As described by Koshioka *et al.*,<sup>70</sup> the fluorescence signal recorded with a confocal microscope is slightly depolarized by the objective due to its high numerical aperture. To account for this experimental artifact, correction factors  $l_1$  and  $l_2$  have been introduced:<sup>70</sup>

$$r = \frac{GF_{\parallel} - F_{\perp}}{(1 - 3l_2)GF_{\parallel} + (2 - 3l_1)2F_{\perp}} \quad (5)$$

The correction factors  $l_1$  and  $l_2$  as well as the factor  $G$ , that compensates for the slightly different detection efficiencies of the two detection channels, were determined experimentally using the reference dyes enhanced green fluorescent protein (EGFP)<sup>58</sup> or rhodamine 110 and TMR, respectively, ( $l_1 = 0.0308$ ,  $l_2 = 0.0368$ ,  $G = 0.99$ ). In detail, the  $G$ -factor is defined as the ratio of the detection efficiencies between perpendicular and parallel polarized fluorescence light. The fluorescence signal  $F$  is obtained from the detected signal by subtracting the appropriate background (scattering) measured in clean water or an unloaded gel.

**2.3.2. Macroscopic transmission imaging (MTI).** We found a linear relation between fluorescence intensity and concentration in the concentration range of 0.1 to 10  $\mu\text{M}$  for all samples. Thus, we can directly determine the relative change in concentration from the image intensity. Especially for the larger dextran molecules, equilibration between the hydrogel and the surrounding solution takes several days. However, for most samples, it was found that measurement times of about 24 h were sufficient to allow diffusion coefficients to be extracted from the data. Some additional longer measurements were performed to capture the long time behavior. Even though the dyes used were relatively photostable and the incident intensity was reduced as much as possible, some photobleaching could be seen for these long measurement times. Thus, a photobleaching correction as described in ref. 71 and 72 was applied: the change in the normalized intensity  $F$  of an area in the solvent far outside the hydrogel, where no significant change in the concentration is expected, could be fitted with a double exponential function:

$$\frac{F(t)}{F(t=0)} = Pe^{-Pt} + Qe^{-qt} \quad (6)$$

The intensity of the region of interest in the gel of every image was then corrected by dividing the original value by the one extracted from the bleach curve.

The hydrogel discs had a quasi-two-dimensional geometry and homogeneous radial diffusion was observed. Thus, by azimuthally averaging all pixels that are a certain distance away from the gel-reservoir interface, a concentration profile for every time step could be determined. Comparison of the concentration profiles with diffusion equations, including appropriate boundary conditions, yields diffusion coefficients (see Section 3.2.1).

The hydrogels were fully swollen and in equilibrium before the measurements and no change in the hydrogel size was expected. However, for some samples we observed a decreasing gel radius of up to 6% within the first hours of the experiments in the bright-field transmission images and the change in radius was taken into account in the analysis. The reason for this is not clear. A change in temperature or an expansion of the sample cell and with that a slight increase in sample thickness might play a role.<sup>73</sup>

**2.3.3. Nuclear magnetic resonance (NMR).** As is usual practice, the diffusion coefficients  $D$  were obtained by fitting the echo amplitudes (integral of the signals between 2.8 and 4.4 ppm) to the following equation:<sup>74,75</sup>

$$\frac{E_i}{E_0} = \exp \left[ -D(\gamma g_i \delta)^2 \left( \Delta_N - \frac{\delta}{3} - \frac{\tau_N}{2} \right) \right] \quad (7)$$

where  $E_i$  and  $E_0$  are the echo intensities at increment  $i$  and with zero gradient applied,  $\gamma$  is the gyromagnetic ratio,  $g_i$  is the gradient amplitude at increment  $i$ ,  $\delta$  is the gradient pulse width,  $\Delta_N$  is the diffusion delay and  $\tau_N$  is the delay between the two magnetic field gradient pulses laying at one side of the echo pulse sequence. For the purpose of comparison, the diffusion coefficients measured in  $D_2O$  were recalculated for  $H_2O$  using the known viscosities of both solvents.<sup>76</sup>

#### 2.4. Models for Brownian dynamics simulations

Brownian dynamics simulations were used to calculate the diffusion coefficients of dextran particles within the polymer network. Inspired by previous investigations,<sup>46,47</sup> we considered simple models of effective spheres for the matrix particles and the dextrans. For this, we used a microscopic model resolving the matrix explicitly and coarse-graining the diffusing polymer coil as an effective soft sphere. There are further underlying model assumptions: (i) the polymer matrix is not resolved on the monomer level, (ii) the matrix structure is derived from a periodic structure, and (iii) explicit hydrodynamic interactions caused by the solvent are ignored.

In order to obtain a systematic insight, the flexibility of the polymer matrix and the softness of the dextran–matrix interaction were modeled on three different levels. A schematic illustration of the models is shown in the Results section (see Section 3.2.2 and Fig. 9). On the first level (also referred to as model 1 in the following), the matrix particles were fixed on a periodic simple-cubic lattice with lattice constant  $a$  providing static steric obstacles for the diffusing dextran molecules. For simplicity, the latter were modeled as effective spheres. On this crude level any fluctuations in the pore sizes were neglected. The repulsive steric interaction between an obstacle  $i$  at position  $\vec{s}_i$  and another particle  $j$  (either tracer or obstacle) at position  $\vec{s}_j$ , separated by the distance  $s_{ij}$ , was modeled as in ref. 47 with a truncated and shifted repulsive Lennard Jones potential (also known as WCA-potential):

$$U_s(s_{ij}) = 4\epsilon_s \left[ \left( \frac{\sigma_{ij}}{s_{ij}} \right)^{12} - \left( \frac{\sigma_{ij}}{s_{ij}} \right)^6 + \frac{1}{4} \right] \quad (8)$$

where  $\epsilon_s = 1k_B T$  ( $\sim 4.05 \times 10^{-21}$  J at 20 °C) and the additive diameter  $\sigma_{ij} = 2R_{\text{obst}}$  for the obstacle–obstacle-interaction and  $\sigma_{ij} = R_{\text{obst}} + R_h$  for the interaction between a matrix obstacle and a tracer of radius  $R_h$ . The cutoff was set at the potential's minimum at  $l_{ij} = 2^{1/6}\sigma_{ij}$ .

For the second level (model 2), we introduced fluctuating matrix particles. The network connectivity was ensured by coupling neighboring matrix particles by harmonic springs. For the harmonic spring potentials, we used Hooke's law:

$$U_{\text{sp}}(s_{ij}) = 0.5k(s_{ij} - s_{0,ij})^2 \quad (9)$$

for two matrix particles  $i$  and  $j$  with their distance at rest  $s_{0,ij}$ . Setting  $k = 2k_B T / (2R_{h,D3})^2$  ( $\sim 0.6$  mJ m<sup>-2</sup>) allowed the dextran D3 to push a gap of its own diameter  $2R_{h,D3}$  through two neighboring matrix particles in rest positions when overcoming an energy of  $1k_B T$ . This parameter is kept fixed in all simulations. Moreover the matrix particles were exposed to thermal fluctuations and repelled each other and the dextran particles *via* steric interactions as in model 1 (eqn (8)). To broaden the pore size distribution, the matrix particles were randomly shifted up to half the lattice constant  $a$  in each direction with respect to their initial positions before attaching undistorted springs between neighboring matrix particles.

At a third level of modeling, two different extensions were tested by changing the dextran–matrix interactions. In model 3a, we replaced the WCA potential for the steric interactions with a softer effective Gaussian potential which is a good model for penetrating polymer coils of different architecture:<sup>77–79</sup>

$$U_G(s_{ij}) = \epsilon_G \exp \left( -\frac{s_{ij}^2}{2b^2} \right) \quad (10)$$

with  $b^2 = (R_i + R_j)^2 / (2 \ln(\epsilon_G / (k_B T)))$ . This relation keeps the potential at  $s_{ij} = R_i + R_j$  for  $1k_B T$ . We used  $\epsilon_G = 12k_B T$  (for more details see S11, ESI†).

In model 3b, an attractive shell with the size of a typical fluorescent dye's radius ( $R_{D0} = 0.55$  nm) was added to the steric repulsion to account for a possible weak sticking of the dextrans to the matrix using a cosine function for a smooth transition:

$$U_{\text{sp}}(s_{ij}) = \begin{cases} 4\epsilon_s \left[ \left( \frac{\sigma_{ij}}{s_{ij}} \right)^{12} - \left( \frac{\sigma_{ij}}{s_{ij}} \right)^6 + \frac{1}{4} \right] - \epsilon_a & s_{ij} \leq l_{ij} \\ -\frac{\epsilon_a}{2} \left[ \cos \left( \frac{\pi(s_{ij} - l_{ij})}{R_{D0}} \right) + 1 \right] & l_{ij} < s_{ij} \leq l_{ij} + R_{D0} \\ 0 & l_{ij} + R_{D0} \leq s_{ij} \end{cases} \quad (11)$$

We obtained  $\epsilon_a = 3.0 \pm 0.3 k_B T$  as fitted value in both investigated systems. This value seems reasonable as it should cause a significant slowdown of the dextrans' motion while still allowing a thermal escape out of the shells.

By tracking the tracer's trajectories, the mean square displacements can be calculated as:

$$\Delta s^2(t) = \langle (\vec{s}(t_0 + t) - \vec{s}(t_0))^2 \rangle \quad (12)$$

For a given sufficiently large elapsed time  $t$ , the long-time diffusion coefficients could then be extracted as:<sup>80,81</sup>

$$D = \lim_{t \rightarrow \infty} \frac{1}{6} \frac{d}{dt} \Delta s^2(t) \quad (13)$$

such that the hindrance factors are  $D/D_0$ .

For a given value of  $a$ , which sets the mean pore size, the hindrance factors for all tracer particles were calculated and this set of simulation data was compared to the experimental data. An optimal value for  $a$  was found by the best fit, using  $a$  as the single fitting parameter. Only in model 3b,  $\varepsilon_a$  was used as a second fitting parameter. For more technical details, see S11 (ESI<sup>†</sup>).

### 3. Results and discussion

The different experimental techniques used here allowed us to estimate the precision of the measurements in different ways. In MTI and NMR, the experiments are conducted by averaging over one gel, calculating therefore the dispersion of the data between different gels.

In MFIS we are able to detect two kinds of dispersion of the data: (i) we measured different spots within the same gel (pixelwise analysis) and (ii) we executed measurements between different gels (different data points in Fig. 12b).

It is known that the hydrogels in practice always exhibit an inhomogeneous cross-link density distribution, causing spatial heterogeneity.<sup>82,83</sup> The scattering of experimental data from various independent measurements, beyond the shot noise limits of the single measurements, indicates the heterogeneity in the gel structure. Spatial heterogeneity on the macroscopic scale is detected by pixelwise analysis. Different locations within the same gel display slightly different results. These feature were visible in all MFIS studies reported below.

#### 3.1. Several populations of guest molecules detected by MFIS

**FCS.** In contrast to the single diffusion times observed in solution, for most of the gel samples we have observed that up to three independent diffusion times are needed to fit the

FCS curves. Differently diffusing species, extending from free molecules just hindered by the limiting pore size ( $t_d \sim 410 \mu\text{s}$ ) up to temporarily trapped particles ( $t_d > 10 \text{ ms}$ ) were found (SI2–4, ESI<sup>†</sup>). Fig. 1a displays a set of image-integrated correlation curves for A488-D10 at different electrolyte conditions which reveal the decreasing fraction of slowly diffusing temporarily trapped particles for increasing salt concentration. Temporary sticking and accumulation of the probe molecules in the hydrogel are indicated by time trace analysis (Fig. 4a). Such tracer–hydrogel interactions already have been studied in the past, showing different effects depending on the chemical structure of the gel, the solvent and the nature of the tracer.<sup>21,25,27</sup>

Interestingly, Vagias and coworkers<sup>21</sup> also found interactions between the hydrogel and different tracers when employing FCS. Although they used another hydrogel than in our study, the different fluorescence intensity between gel and solution is clearly shown by them.

A simple binding model was applied to describe the observed equilibrium fractions of mobile and trapped probe molecules ( $x_{\text{bound}}$ ), where  $f_{\text{free}}$  is the activity coefficient for free molecules and  $K_d'$  the effective binding constant (see S1.7, ESI<sup>†</sup>):

$$x_{\text{bound}} = \frac{f_{\text{free}} K_d'}{1 + f_{\text{free}} K_d'} \quad (14a)$$

It was assumed that the activity of the freely diffusing (mobile) species is most affected by the ionic strength of the solvent. The Debye–Hückel equation<sup>84</sup> describes the dependency of the activity coefficient,  $f_{\text{free}}$ , on the charge,  $Z_i$ , the effective radius of the ion,  $R_i$ , and the ionic strength,  $I$ , in the limit of low salt concentrations:

$$f_{\text{free}} = 10^{-\frac{AZ_i^2\sqrt{I}}{1 + BR_i\sqrt{I}}} \quad (14b)$$

with tabulated values<sup>84</sup> for the constants  $A = 0.507 \text{ mol}^{-1/2} \text{ dm}^{3/2}$  and  $B = 3.28 \text{ nm}^{-1} \text{ mol}^{-1/2} \text{ dm}^{3/2}$  for aqueous solution at 22.5 °C. A combination of eqn (14a) and (14b) can be fit to the equilibrium fraction of trapped molecules as a function of the ionic strength. The fit shown in Fig. 1b yields  $Z_i \approx 3$ , which is in good agreement with the estimated mean number of

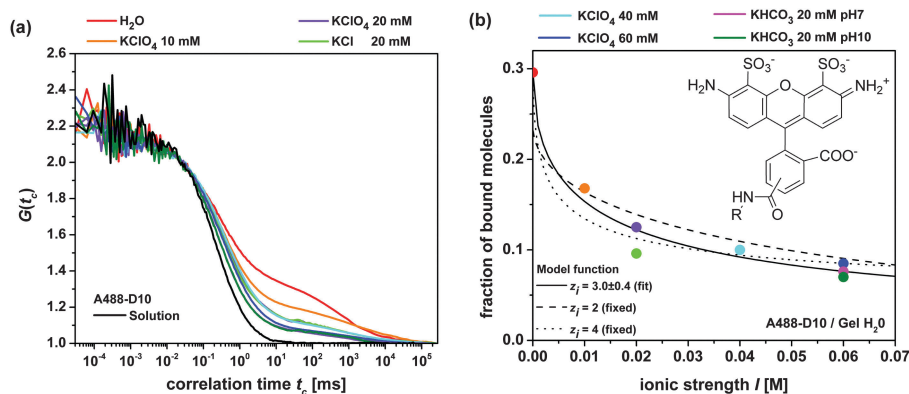


Fig. 1 (a) Image-integrated normalized correlation curves for A488-D10 in hydrogels at different salt conditions, (b) decreasing fraction of slow, temporarily bound molecules for A488-D10 in the hydrogel with increasing ionic strength  $I$ . A fit of eqn (14) yields  $Z_i = 3.0 \pm 0.4$ ;  $K_d' = 0.42 \pm 0.03$ ;  $R_i = (0.7 \pm 0.5) \text{ nm}$ . The inset shows one possible mesomeric structure and charge distribution of Alexa488.

charges per labelled dextran, estimated as follows. D10 samples have  $\sim 5$  labelling sites per molecule. The specified mean degree of labelling ( $\text{DoL}_{\text{av}}$ ) of the investigated A488-D10 samples is 1, if the unlabelled dextran molecules are also considered. However, considering only labelled dextrans in a first approximation of random labelling, we can expect around 1.5 dyes per labelled and thus detected dextran (for more details of this calculation, see S1.3, ESI $\dagger$ ), which corresponds to a mean charge  $Z_i(\text{A488-D10}) \approx 3$ . For the higher salt concentrations, the Debye length  $\kappa^{-1}$  is of the order of the macromolecule's dimension ( $\kappa^{-1} \approx 1.4$  nm for  $I = 0.05$  M), producing conditions beyond some of the approximations made to derive eqn (14b). Nevertheless, the fit shown in Fig. 1b describes the experimental data sufficiently well.

The analysis reveals that mainly the presence or screening of charges determine the sticking behavior of the probe molecules and not the kind of anion as suggested by the Hofmeister series.<sup>85,86</sup> In particular, perchlorate, chloride or hydrogen carbonate ions at the same ionic strength had a comparable influence on the diffusion properties of the studied samples (see Fig. 1b).

**Fluorescence anisotropy.** To compare the restricted motion of A488-D10, TMR-D10 and FLU-D10 in the hydrogel to its behavior in solution, we performed measurements of steady state anisotropy  $r$  and time resolved anisotropy  $r(t)$  for each pixel. For this, a possible distribution of  $r$  due to the heterogeneous environment needed to be separated from shot-noise broadening. Thus, a plot of  $r$  vs. number of detected photons,  $N_F$ , was analyzed (Fig. 2a), and the mean anisotropy,  $\langle r \rangle$  was calculated:<sup>87</sup>

$$r = \langle r \rangle \pm \frac{1}{3} \frac{(2 + \langle r \rangle) \sqrt{(1 - \langle r \rangle)(1 + 2\langle r \rangle)}}{\sqrt{N_F}} \quad (15)$$

It is clear that, on average, A488-D10 exhibits a higher anisotropy in the gel than in aqueous solution. This can be attributed to a temporary trapping of the solute in the matrix network. The plotted values for  $r$  in the gel are pixel-averages where

about 30% of molecules were trapped for this sample (Fig. 1b). During the measurement time of 1800 s, many probe transits are averaged, so that the anisotropy reports on the average trapping probability. In our samples different pixels display different anisotropies, so that the width of the distribution significantly exceeds the shot-noise broadening as found in the solution measurement. This can only be explained by the spatial heterogeneity of the hydrogel.

To study probe-polymer interactions inside the gel matrix,  $r$  measurements were performed for A488-D10 under different conditions ( $\text{KClO}_4$  10 mM, 20 mM, 40 mM, 60 mM;  $\text{KCl}$  20 mM; potassium carbonate buffer pH 7, 20 mM and pH 10, 20 mM, for TMR-D10 and FLU-D10 in  $\text{H}_2\text{O}$ , in potassium carbonate buffer 20 mM pH 10 and in Tris buffer 50 mM pH 7.5). The 2D  $r$ - $N_F$  plots for all conditions are shown in S7 (ESI $\dagger$ ). Fig. 3 shows the relation of the ratio of  $r$  in the hydrogel to  $r$  in different aqueous electrolyte solution and the fraction of trapped particles,  $x$ , which is directly calculated from FCS curves by applying eqn (4) (for values see Table S8, ESI $\dagger$ ).

In a two-component system the additive behavior of anisotropies predicts a linear dependence of  $r_{\text{gel}}$  on the fraction of the trapped species  $x$ :  $r_{\text{gel}} = xr_{\text{trapped}} + (1-x)r_{\text{sol}}$ . To take into account different initial solution anisotropies of the differently labeled probe molecules relative anisotropies  $r_{\text{gel}}/r_{\text{sol}}$  are plotted in Fig. 3. By fitting a line to the data and using  $r_{\text{sol}} = 0.037$  (Fig. 2) we estimate mean  $r_{\text{trapped}} = 0.10 \pm 0.01$  for A488-D10. This is much less than the fundamental anisotropy of A488 ( $r_0 = 0.37$ ) which would be expected for the completely immobilized dye. The low density of labels renders energy transfer between identical chromophores an unlikely cause for the reduced anisotropy, leaving partial mobility of the dye even in the trapped environment as most probable explanation.

**Fluorescence time traces.** Time-traces of A488-D10 at low concentration in the hydrogel were investigated to further analyze the sticking behavior (Fig. 4a). Temporary sticking and accumulation of the probe molecules in the hydrogel are indicated by relatively long dwell times (up to seconds) and count rates which are significantly above average, both of

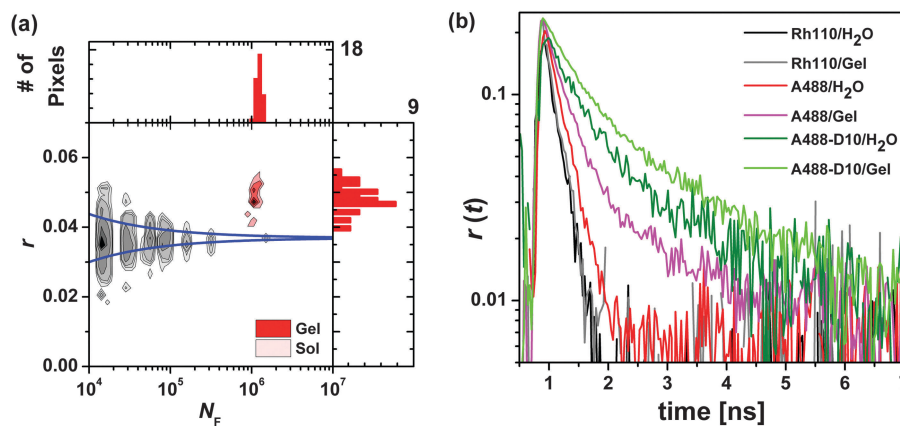


Fig. 2 (a) Anisotropy  $r$  vs. photon number  $N_F$  in different time windows for A488-D10 in water (gray contour lines) and in hydrogel (red contour lines) with one-dimensional projections for the gel data. The time window for the gel data was 1800 s. The theoretical shot-noise limits of  $r$  are calculated with eqn (15) with  $\langle r \rangle = 0.037$  (blue lines). (b) Anisotropy decays,  $r(t)$  for Rh110, A488 and A488-D10 in  $\text{H}_2\text{O}$  and gel/ $\text{H}_2\text{O}$ .

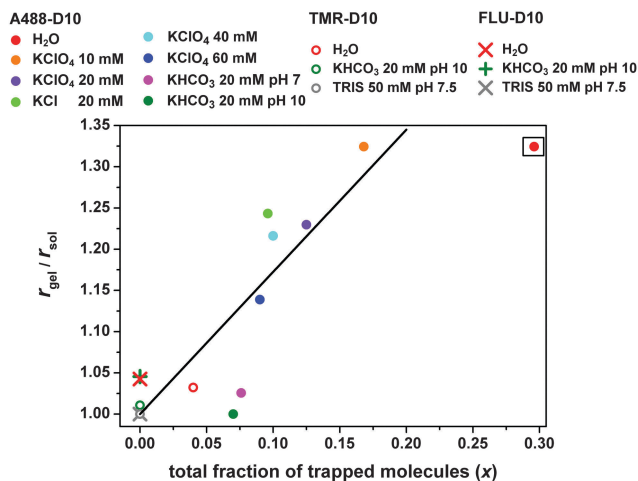


Fig. 3 Average anisotropy ratio,  $r_{\text{gel}}/r_{\text{sol}}$  as a function of the fraction of trapped particles derived from FCS measurements for A488-D10 (see Fig. 1), TMR-D10 and FLU-D10. Linear extrapolation (without H<sub>2</sub>O value) yields  $r_{\text{gel}}/r_{\text{sol}} = 2.7 \pm 0.3$  for  $x = 1$ .

which are not observed for molecules freely diffusing in solution (Fig. 4a). A strong correlation between the fraction of the trapped molecules is revealed by the slow decay between 10 ms and several seconds and the mean count rate for this time range in the corresponding fluorescence correlation curves (Fig. 4b).

The interaction of A488-D10 with the matrix is revealed by several different observations: first, a reduction of the fluorescence lifetime ( $\tau_{\text{gel}}/\tau_{\text{sol}} \approx 0.95$ ), mainly attributed to quenching since a change in radiative lifetime due to refractive index differences between gel and solvent is expected to only account for 1/3 of the effect ( $\tau_{r(\text{gel})}/\tau_{r(\text{sol})} \approx 0.987$ , see S1.6, ESI<sup>†</sup>),<sup>88,89</sup> and, second, an increased anisotropy ( $r_{\text{sol}} = 0.037$ ,  $r_{\text{gel}} = 0.049$ ) with broadened distribution inside the gel (see Fig. 2 and 3). Third, the apparent brightness  $B_{\text{app}}$  of A488-D10 in the hydrogel, obtained as the ratio of detected count rate to the apparent number of particles  $N$  (taken from the FCS amplitude, eqn (4)), is significantly lower than  $B$  measured in solution ( $B_{\text{app}}/B \approx 0.37$ ) which is not consistent with the weak dynamic quenching indicated by the small change in fluorescence lifetime. One possible explanation could be that a fraction of the molecules are

trapped on a longer time scale ( $> 1$  min) which results in a virtually uncorrelated background reducing the correlation amplitude. Taking long term trapping into account for the highly interacting A488-D10, an effective concentration of trapping sites in the range from 10 to 50 nM can be deduced for low salt conditions (detailed discussion in the S1.4 and S1.5, ESI<sup>†</sup>). The observation of systematically higher fluorescence intensities inside the loaded gel than in the surrounding solution supports the idea of the enrichment of probe molecules in the gel (for details see S1.1 and S6, ESI<sup>†</sup>).

## 3.2. Mobile guest molecules

### 3.2.1. Experimental results

**MFIS.** As already discussed, the analysis of FCS correlation curves as displayed in Fig. 1a revealed different populations of guest molecules with differing diffusion times. In this section, we only consider the freely diffusing species with the smallest diffusion time. With MFIS, the hydrogel was studied in deionized water as well as in 20 mM potassium carbonate buffer at pH 10. Significantly different results were found for the two experimental conditions. These differences can be explained by a solvent dependent degree of swelling of the hydrogel (see sample details, Section 2.1.1). The diffusion coefficients from FCS experiments are shown in Table 3.

**MTI.** Fig. 5a shows an example set of fluorescence images at the beginning and the end of an MTI experiment of A488-D10 diffusing into a hydrogel disc. Due to the influx of fluorescent particles into the polymer hydrogel, the fluorescence intensity inside the hydrogel increases with time. A higher intensity inside the hydrogel is clearly visible at the end of the measurement. This indicates enhanced fluorescence of the dyes inside the gel and/or an attraction of the dye to the hydrogel. As expected, a variation of the particle concentration between 0.1  $\mu\text{M}$  and 10  $\mu\text{M}$  did not change the diffusion coefficient.

In these experiments the two faces of the hydrogel discs were not accessible to the solvent. Thus, the samples can be described as infinitely long cylinders in a reservoir of dye or dextran in solution, *i.e.* a quasi two-dimensional geometry with radial diffusion. Assuming azimuthally homogeneous diffusion, for every fluorescence image, the azimuthally averaged

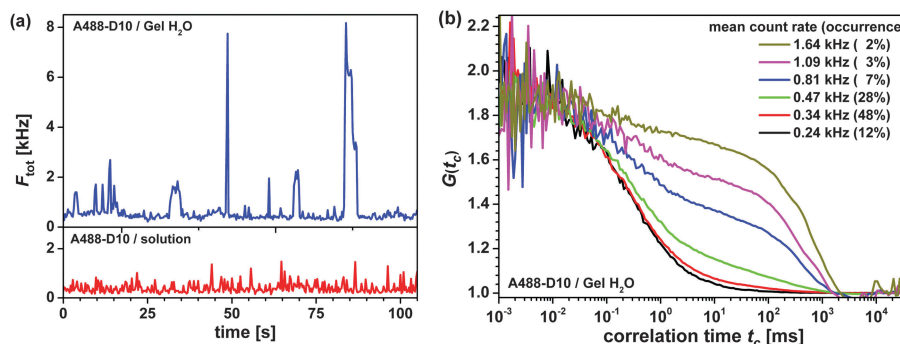
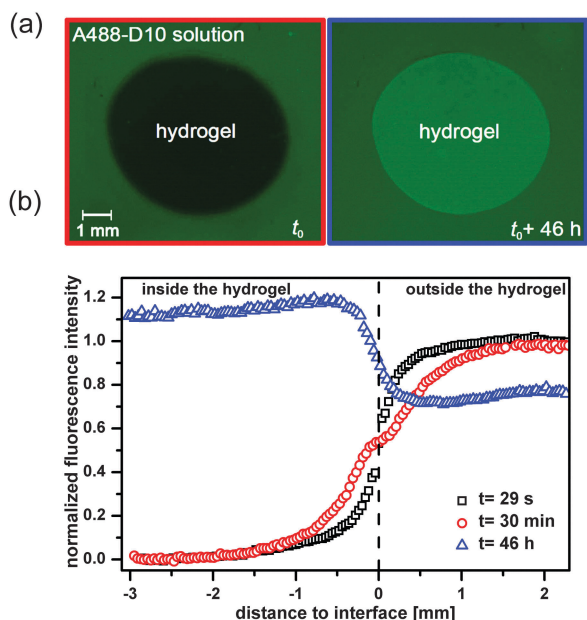


Fig. 4 (a) Fluorescence time traces (sum of perpendicular and parallel channel) for a single pixel in the image of A488-D10 in solution and in the gel in water conditions, (b) correlation curves of count rate selected subsets of the trace (for details see S5, ESI<sup>†</sup>).

**Table 3** Diffusion coefficients of free dye and dextran conjugates in solution,  $D_{\text{sol}}$ , and in the hydrogel,  $D_{\text{gel}}$ , at 22.5 °C

| Sample   | Dye <sup>a</sup> | $M_w^b$<br>[kDa] | $R_h^c$<br>[nm] | $D_{\text{sol}}$<br>[10 <sup>-6</sup> cm <sup>2</sup> s <sup>-1</sup> ] | $D_{\text{gel}}$<br>[10 <sup>-6</sup> cm <sup>2</sup> s <sup>-1</sup> ] |
|----------|------------------|------------------|-----------------|---|---|
| Free dye | A488             | 0.53             | 0.56            | 3.69 ± 0.05   | 2.7 ± 0.1   |
|          | TMR              | 0.39             | 0.56            | 3.45 ± 0.07   | 2.6 ± 0.1   |
|          | FLU              | 0.33             | 0.54            | 4.33 ± 0.09   | 3.9 ± 0.1   |
| D3       | A488             | 3                | 1.7 ± 0.1       | 1.05 ± 0.02   | 0.59 ± 0.02   |
|          | TMR              |                  |                 | 1.13 ± 0.02   | 0.62 ± 0.02   |
|          | FLU              |                  |                 | 1.45 ± 0.03   | 1.24 ± 0.04   |
| D10      | A488             | 10               | 3.1 ± 0.2       | 0.64 ± 0.01   | 0.32 ± 0.02   |
|          | TMR              |                  |                 | 0.99 ± 0.02   | 0.47 ± 0.02   |
|          | FLU              |                  |                 | 0.60 ± 0.02   | 0.54 ± 0.02   |
| D40      | TMR              | 40               | 6.0 ± 0.3       | 0.38 ± 0.01   | 0.10 ± 0.01   |
|          | FLU              |                  |                 | 0.32 ± 0.01   | 0.18 ± 0.03   |
| D70      | TMR              | 70               | 7.9 ± 0.4       | 0.33 ± 0.01   | 0.083 ± 0.004   |
| D500     | FLU              | 500              | 20 ± 2          | 0.107 ± 0.002   | 0.04 ± 0.02   |
|          |                  |                  |                 |   |   |
| D2000    | TMR              | 2000             | 40 ± 4          | 0.068 ± 0.002   | —   |
|          | FLU              |                  |                 | 0.060 ± 0.001   | —   |

<sup>a</sup> A488 and TMR samples measured in deionized water, FLU in 20 mM potassium carbonate buffer at pH10. <sup>b</sup> Molecular mass  $M_w$  as obtained from manufacturer. <sup>c</sup> Hydrodynamic radii  $R_h$  for free dyes are calculated from reported diffusion coefficients *via* Stokes–Einstein equation,<sup>90–93</sup>  $R_h$  of dextran conjugates are obtained from a fitted Flory scaling law to our MFIS and NMR data (see Fig. 8). Errors for  $D_{\text{sol}}$  and  $D_{\text{gel}}$  are standard errors of the averages from multiple measurements, errors for  $R_h$  are 68% confidence intervals ( $\pm 1\sigma$ ) from the fit.



**Fig. 5** (a) Example fluorescence images at the beginning ( $t_0$ ) and the end of an experiment, (b) intensity–distance profiles for 29 s, 30 min and 46 h after contacting a cylindrical polymer hydrogel with A488-D10 solution.

intensity profiles were determined. Typical intensity–distance profiles for three times are displayed in Fig. 5b. The 46 h data illustrate that the fluorescence intensity in the gel is higher than in solution.

Diffusion equations for radial diffusion in an infinite cylinder with radius  $R_d$  suspended in an infinite reservoir with a diffusion coefficient  $D_{\text{gel}}$  yield a radial concentration profile  $c(s,t)$  of the diffusing substance with the radial position  $s$  inside the infinite cylinder:<sup>94</sup>

$$c(s,t) = c_\infty + \left( \frac{c_i - c_\infty}{2D_{\text{gel}}t} \right) e^{-\frac{s^2}{4D_{\text{gel}}t}} \int_0^{R_d} e^{-\frac{s'^2}{4D_{\text{gel}}t}} I_0 \left( \frac{ss'}{2D_{\text{gel}}t} \right) s' ds' \quad (16)$$

with the modified Bessel function of the first kind of order zero,  $I_0$ , and the initial and final concentrations  $c_i$  and  $c_\infty$ , respectively.

Analysis of the complete concentration profiles is nontrivial because if the hydrogel edge is not perfectly perpendicular, this can lead to scattering and edge effects which will influence the shape of the measured concentration profiles. We thus first considered a more robust approach and analyzed the temporal increase in concentration in the center of the hydrogel. To enhance statistics, we averaged over an area of 0.2 mm by 0.2 mm in the center of the hydrogel. This area is small compared to the overall size of the gel ( $R_d \approx 3.5$  mm). One typical dataset for the increase of A488-D10 in the center of a cylindrical hydrogel is shown in Fig. 6.

From eqn (16) an expression for  $s = 0$  was derived:<sup>94</sup>

$$c(t) = c_i + (c_\infty - c_i) e^{-\frac{R_d^2}{4D_{\text{gel}}(t+t_0)}} \quad (17)$$

An imperfectly perpendicular hydrogel edge and potential scattering from the gel edge will lead to a broadened start profile (Fig. 5). This was accounted for by adding a time-offset  $t_0$  in eqn (17). This equation was fitted to the time evolution of the intensity in the center of the hydrogel. This resulted in very good agreement with the data (see Fig. 6). As the gel radius plays an important role in the determination of  $D_{\text{gel}}$ , we fitted all datasets with both the initial and the final radius (given in Section 2.3.2) and estimated  $D_{\text{gel}}$  to be between the values we get from these fits (Table 4).

Since the reservoir in the experiments was finite, the above model does not perfectly describe the experimental conditions. In the experiments, the volume of the solution surrounding the

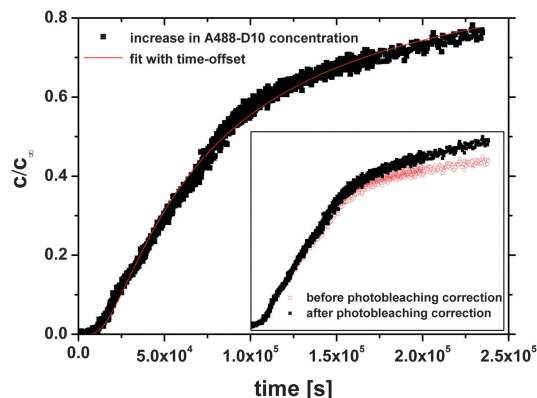


**Fig. 6** Increase in A488-D10 concentration in the center of a hydrogel disc with time. The inset shows the original data (open circles) and the data after a photobleaching correction has been applied (closed squares).

**Table 4** Diffusion coefficients of A488 free dye and dextran conjugates in the hydrogel at 23 °C measured by MTI. Errors for  $D_{\text{gel}}$  are standard errors of the averages from multiple measurements

| Sample   | Dye  | $D_{\text{gel}}$ [ $10^{-6}$ cm <sup>2</sup> s <sup>-1</sup> ] |
|----------|------|--|
| Free dye | A488 | 3.2 ± 0.1  |
| D3       | A488 | 0.73 ± 0.02  |
| D10      | A488 | 0.42 ± 0.01  |

gel was about 11 times the cylinder volume. This should result in a homogeneous final dye concentration  $c_{\infty} \approx 0.92c_i$  in both the gel and reservoir. This has not been observed (Fig. 5). Thus we considered a second model; diffusion into a cylinder from a stirred solution of limited volume.<sup>94</sup> The fitting results from this model were compared to those from the above model (eqn (16)). The second model was found to describe the data for short and intermediate measurement times, but failed to describe the long time behavior. The model suggests that saturation between cylinder and reservoir should be achieved much faster than seen in the experiments. This discrepancy could be due to an attractive interaction between the hydrogel and the diffusing molecules as indicated by the MFIS experiments. In line with this idea is the observation that for all measurements with Alexa-labelled particles, the fluorescence intensity of the hydrogel was higher than that of the surrounding solution at the end of the measurement (Fig. 5). If the particles are attracted to the hydrogel, they will preferentially diffuse into the gel even after the concentration difference between gel and reservoir is balanced. This corresponds to a larger effective reservoir as described by eqn (16), which is based on an infinite reservoir.

**NMR.** Diffusion coefficients of unlabelled dextrans in D<sub>2</sub>O and inside the hydrogel were extracted from the NMR measurements using eqn (7) to fit the echo amplitudes. For D40 in the hydrogel, one typical decay curve and the corresponding fit using eqn (7) is shown in Fig. 7 (for more details see S10, ESI†).

Very good agreement between experimental data and the fit can be observed. The resulting diffusion coefficients (average of three measurements with varying gradient length) are shown in Table 5.

**Summary.** Although all applied techniques probe different length scales of the sample, for the same conditions they yield

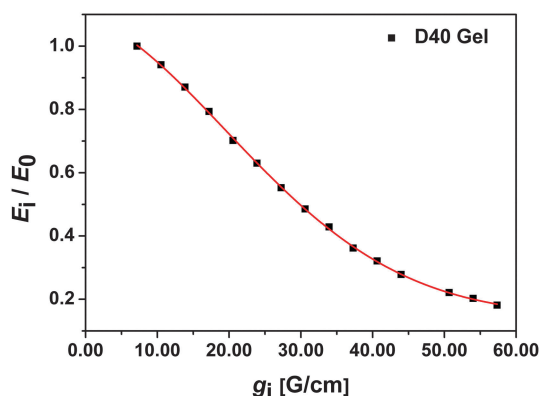


**Fig. 7** NMR data and fit using eqn (7) for unlabelled dextrans (40 kDa) in the hydrogel. The data was normalized.

**Table 5** Diffusion coefficients of unlabelled dextran in solution,  $D_{\text{solution}}$ , and in the hydrogel,  $D_{\text{gel}}$ , at 23 °C measured by NMR

| Sample | Dye  | $R_h^a$ [nm] | $D_{\text{solution}}$ [ $10^{-6}$ cm <sup>2</sup> s <sup>-1</sup> ] | $D_{\text{gel}}$ [ $10^{-6}$ cm <sup>2</sup> s <sup>-1</sup> ] |
|--------|------|--------------|---|--|
| D3     | unl. | 1.7 ± 0.1    | 1.37 ± 0.01   | 0.80 ± 0.01  |
| D10    | unl. | 3.1 ± 0.2    | 1.158 ± 0.003   | 0.38 ± 0.01  |
| D40    | unl. | 6.0 ± 0.3    | 0.451 ± 0.003   | 0.110 ± 0.003  |

<sup>a</sup> Hydrodynamic radii  $R_h$  from  $D_{\text{solution}}$  (free dye) or fitted power law (dextran conjugates, from experimental data, see Table 3). Errors for  $D_{\text{solution}}$  and  $D_{\text{gel}}$  are standard errors of the averages from multiple measurements, errors for  $R_h$  are 68% confidence intervals ( $\pm 1\sigma$ ) from the fit.

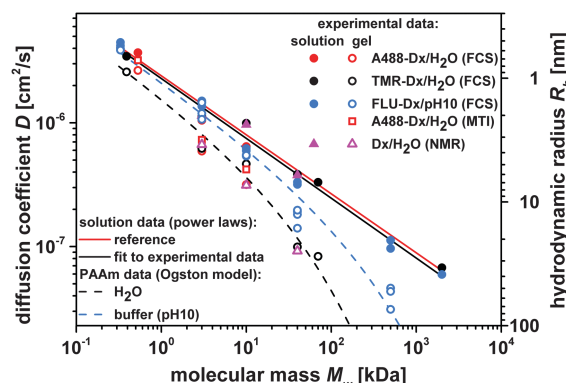


**Fig. 8** Experimental diffusion coefficients  $D$  at 22.5 °C and (for solution data) hydrodynamic radii  $R_h$  for equivalent spheres as estimated by the Stokes–Einstein equation. Solution data (filled symbols) were approximated by the Flory scaling law (red line,  $R_h$  [nm] =  $(1.01 \pm 0.07) \times (M_w$  [kDa])<sup>0.48±0.02</sup>), and compared to reference data (black line,  $R_h$  [nm] =  $(0.96 \pm 0.13) \times (M_w$  [kDa])<sup>0.48±0.04</sup>, see S9, ESI†).<sup>90,95,96</sup> Dashed lines represent fits of the Ogston model (black: H<sub>2</sub>O, blue: buffered solution at pH 10; for parameters see Table 6) to the gel data (open symbols).

remarkably consistent diffusion coefficients, which are displayed in Fig. 8. Fits to the Flory scaling law were used to determine the hydrodynamic radii  $R_h$  (also see S9, ESI†) of the dextrans in solution. As expected, the diffusion coefficients of all our guest molecules decay markedly with increasing molecular weight and the results for all methods agree quantitatively. The heterogeneity in the gel structure is indicated by the scatter of the gel data around the fit curve from various independent measurements beyond the shot noise limit.

**3.2.2. Comparison with Ogston theory.** Besides adsorption or temporary binding phenomena, the hindrance of diffusion, *i.e.* a reduction of the macroscopic diffusion coefficient inside the matrix with respect to the bulk diffusion coefficient is a fundamental property characterizing the transport behavior of particles within the matrix. Diffusion of solutes inside the pores has been approximated by many models.<sup>97–99</sup> Here we applied a simple fiber network theory. This model goes back to Ogston *et al.*<sup>35</sup> and describes a hydrogel as a network of randomly distributed fibers. Based on this model, the hindrance factor is

$$H = \exp\left(-\sqrt{\varphi\left(1 + \frac{R_h}{R_f}\right)^2}\right) \quad (18)$$

where  $R_f$  is the radius and  $\varphi$  the volume fraction of the fibers in the gel and  $R_h$  the hydrodynamic radius of the diffusing species.

The important assumptions behind this model are known: (i) the solute/fiber interaction is purely hard-sphere in nature, (ii) the fibers are infinitely long and were placed randomly in the matrix, and (iii) the solute concentration is very low, so that solute–solute interactions are negligible in both phases. It is clear that such approach can only be a crude approximation of the real physical effects that are governing the translocation in the matrix in our system. Nevertheless, Ogston's model yields a convenient and simple analytic expression to analyze fundamental trends. Moreover, such approach implies the use of effective parameters, permitting in terms of the volume fraction ( $\varphi$ ), to obtain reasonable results in comparison to the experimental values as estimated from analysis of the swelling behavior (see Section 2.1.1).

As expected and shown in Fig. 8, the diffusion coefficient  $D$  decreases with dextran size, with the decrease being more pronounced in the gel. Thus, the hindrance factor,  $H = D_{\text{gel}}/D_{\text{sol}}$ , will also decrease with increasing hydrodynamic radius  $R_h$  of the dextrans (see Fig. 12).

Dashed lines in Fig. 8 represent the curves calculated with the Ogston model (eqn (18)) using the fit parameters listed in Table 6.

**Table 6** Results from fitted model function with standard errors and the experimentally determined polymer volume fraction ( $\varphi$  in the swollen hydrogel)

|                                |                  | TMR-Dx/H <sub>2</sub> O | FLU-Dx/pH 10        |
|--------------------------------|------------------|-------------------------|---------------------|
| Fiber network model (eqn (18)) | $\varphi$ (exp.) | $0.0390 \pm 0.0004$     | $0.0150 \pm 0.0001$ |
|                                | $\varphi$        | $0.06 \pm 0.03$         | $0.005 \pm 0.007$   |
|                                | $R_f$ [nm]       | $1.4 \pm 0.5$           | $1.3 \pm 1.1$       |

The agreement with our data is already very good. Using newer, comparable models (such as the Amsden-model<sup>97</sup>) did not noticeably improve agreement with our data (thus not shown in Fig. 8).

### 3.2.3. Comparison with Brownian dynamics simulations.

While the Ogston model provides a simple analytical formula to describe the trends for the dextran dynamics with an effective excluded volume, we now apply our Brownian dynamics simulations (see Section 2.4) for a more detailed modeling approach. Different approaches to model a hydrogel have been used in previous works. When investigating the swelling behavior of a gel, Linse and coworkers<sup>36–39</sup> and Holm and coworkers<sup>40–42</sup> resolved the individual monomers of the gel network. However the dynamics of tracer particles through the network was not performed within this level of modelling. Addressing tracer motion within monomer-resolved modelling requires much more computational resources in particular for long-time diffusion. Also the fitting procedure would require several sets of runs. Therefore we leave monomer resolved studies to future work. Instead we decided to follow the more coarse-grained approach by Zhou and Chen.<sup>47</sup> This type of modeling provides a simple and systematic framework in which to include different physical effects, namely the mobility of the matrix particles (*i.e.* fluctuations in the matrix structure), the effective dextran–matrix excluded volume, and sticky attractions. The matrix–dextran interactions are expected to play a key role in spreading the delay times of the diffusive process of the dextran molecules through the matrix. Fig. 9 shows schematic two-dimensional representations of the three-dimensional simulations on the three different levels that were used to explain the experimental data.

In qualitative terms, one would expect increasing agreement between the simulation and experimental data as we increase

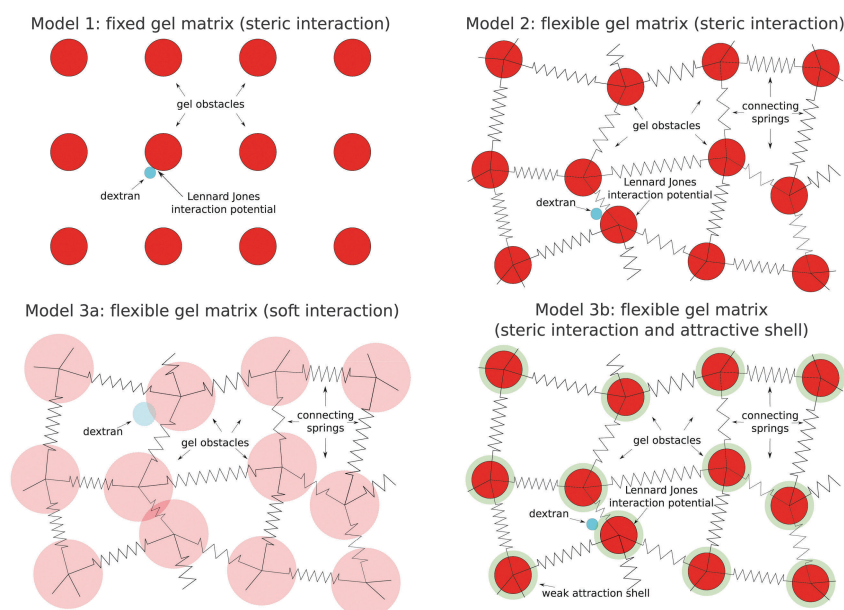


**Fig. 9** Four models for the dextran–matrix system. Model 1: fixed gel matrix (steric interaction, eqn (8)), model 2: flexible gel matrix (steric interaction, eqn (8)), model 3a: flexible gel matrix (soft interaction, eqn (10)) and model 3b: flexible gel matrix (steric interaction and attractive shell, eqn (11)). The sketches illustrate two-dimensional representations of the three-dimensional models used for the simulations.

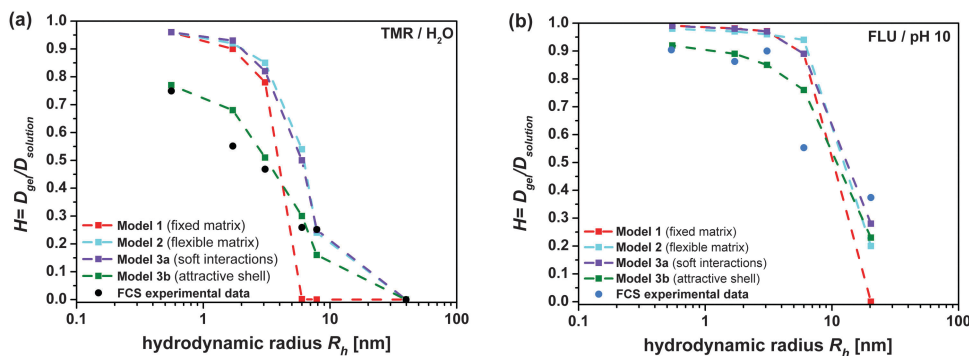


Fig. 10 Comparison between FCS experimental data and Brownian dynamic simulations with 4 different models for TMR-dextran in water conditions (a) and FLU-dextran in 20 mM potassium carbonate buffer at pH 10 (b).

the level of complexity. This is indeed what is observed and displayed in Fig. 10, where the different simulation results are compared to FCS data. In model 1, hard matrix particles are fixed on simple cubic lattice sites, providing a uniform matrix with just one pore size. This results in a very sharp drop in the hindrance factor when the dextran's size is increased to this pore size. Introducing elastically connected matrix particles (model 2) broadens the pore size distribution and leads to a slower decrease of the hindrance factors with dextran size, as expected. However, this decrease is still too sharp compared to the experimental data. Softening the interactions by changing the interaction potentials from WCA to a Gaussian potential (model 3a) shows an even lower, yet still too distinct decrease, of the hindrance factor with increasing dextran size. The agreement is still unsatisfactory. Especially the hindrance of the smaller dextrans is too weak in the previous approaches. When these small dextrans collide with matrix particles, they can easily find another way to pass due to their small size.

The introduction of an attractive contribution in the matrix-guest interaction (model 3b) is found to be crucial to describe the observed slow decay with increasing dextran sizes. If the smaller dextrans collide with matrix particles in this model, they can still find another path to pass. However, they are more likely to first become stuck resulting in a slowdown even for small dextrans.

Model 3b is the only one which includes a repulsive interaction and an attractive shell and it is the best representation of our experimental data. Additional simulations performed within model 3b using a Gaussian softened core showed a similar fit quality as that with a WCA-core. The results show that, within the framework of the model classes considered here, an effective attraction is needed to describe the spreading of the dynamics correctly given the statistical uncertainties of the experimental data. The origin of this attraction still needs to be resolved. For specific simulation parameters see the Table S11 (ESI<sup>†</sup>).

### 3.3. Estimation of the average pore size

The theoretical study permits an estimation of the average pore size of the investigated hydrogel in the two experimental environments. We optimized for the *a priori* unknown average pore size by fitting the simulated hindrance factors to the experimental data. Since the positions of all matrix particles in the BD-simulation

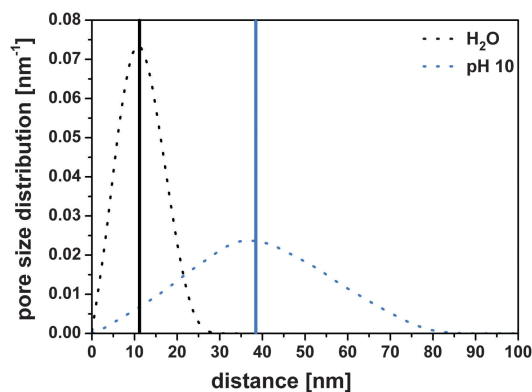


Fig. 11 The distribution of the free space between connected matrix particles (dots) in the BD simulation and the average pore size (bars) of the polymer matrix in both experimental conditions. It is based on the final set of parameters after the fit within the applied model 3b. Black dots correspond to H<sub>2</sub>O, blue dots to 20 mM potassium carbonate buffer at pH 10 (for details see text).

are known, one can estimate the size of a specific pore in the gel as the center-to-center distance of two neighboring matrix-particles minus the matrix-particle-diameter. The decision which matrix particle pairs have to be counted as 'neighbors', is subject to a certain degree of arbitrariness. We chose to consider all particle pairs that are connected with springs, therefore possibly overestimating the correct value by neglecting close, but unconnected, matrix particle-pairs. Fig. 11 shows this distribution for both investigated conditions calculated using model 3b.

We obtained an average value of  $11 \pm 1$  nm for gels in water and  $38 \pm 3$  nm for gels in buffer at pH 10 for the final set of parameters after the fit. While this average pore size is an output from fitting the simulated hindrance factors to the experimental data, the shape of the distribution is rather an input as the width of this distribution (standard deviation  $\sigma = 5$  nm for water,  $\sigma = 16$  nm for pH 10 in Fig. 11) scales with the average value as defined in the models. The average values are in the same order of magnitude as calculated from swelling experiments, where we estimated 5.7 nm and 7.8 nm, respectively, assuming ideal solvent quality, homogeneous cross-linking densities and Gaussian distribution of chain lengths (see Section 2.1.1). In H<sub>2</sub>O both results differ by less than a factor of 2.

We now compare the results of our gel ( $[T] = 0.04 \text{ g ml}^{-1}$ ,  $C_R = 0.035$ ), obtained in water conditions, with literature values for gels with similar composition. Significant discrepancy between pore size values resulting from scanning electron microscopy SEM (10–20  $\mu\text{m}$ )<sup>32–34</sup> and swelling analysis (2.0 nm) was reported.<sup>33</sup> When using SEM, the structure of the gel may become damaged during the freeze-drying processes, resulting in systematically too large pore sizes. In our study, we measured under native conditions without disturbing the gel matrix structure thus circumventing this problem.

In gel electrophoresis with DNA as a cylindrical tracer molecule,<sup>23,30,31</sup> pore sizes between 5.9 and 133 nm are reported for gels with similar composition to ours. The hydrodynamic radius of the DNA was not measured directly but calculated using different models which is known to be an intrinsic problem. Approximating DNA by a sphere becomes more reasonable for shorter DNA molecules. Therefore it is notable, that the electrophoresis study using the shortest DNA<sup>30</sup> matches our result the best.

Very early work of polyacrylamide gels, using electrophoresis of proteins<sup>29</sup> in phosphate buffer, pH 7 ( $[T] = 0.06 \text{ g ml}^{-1}$ ,  $C_R = 0.05$ ) and chromatography of proteins<sup>28</sup> in water ( $[T] = 0.065 \text{ g ml}^{-1}$ ,  $C_R = 0.02$ ) agree well with our results, yielding 8.5 nm and 2.25 nm, respectively. In addition, recent studies<sup>96</sup> based on dynamic light scattering revealed mesh sizes of the same order of magnitude for polyacrylamide hydrogels of about 15 nm and for poly(*N*-isopropylacrylamide) of about 19 nm.

## 4. Combined results and conclusions

All data for the hindrance factor  $H$  obtained from the three different and independent methods we have applied are displayed and compared to Brownian dynamics simulations performed with model 3b in Fig. 12. For the MTI measurements, the average values of  $D_{\text{sol}}$  from NMR and MFIS were used to scale the data, as they could not be measured with this technique.

We have shown that the long time diffusion coefficients of dextran molecules moving in solution and in a polyacrylamide gel

matrix determined on different length scales by using multiparameter fluorescence image spectroscopy (MFIS), macroscopic transmission imaging (MTI) and nuclear magnetic resonance (NMR) are consistent. The measured diffusion coefficients decrease with increasing molecular weight and fall on a master curve. This supports the reliability of our data set, which might thus serve as possible calibration data for future experiments and theories.

In addition, although our results could be described by the Ogston model (Fig. 12), a more realistic model of a flexible gel matrix was applied to describe the experimental data and to estimate the average pore size in the gel. The simulated average pore sizes of 11 nm (water) and 38 nm (pH 10) agree reasonably well with estimations from swelling theory of 5.7 nm and 7.8 nm, respectively. Within the experimental error bars and the limitations of the applied models, our results for the gel equilibrated in water are in good agreement with published studies employing comparable globular macromolecular probes (2.25 nm<sup>28</sup> or 8.5 nm<sup>29</sup>) as well as with light scattering investigations (15 nm)<sup>96</sup> in native gels with similar composition.

Combining experiments and simulations enabled us to achieve a better understanding of the effects determining the diffusion of molecules in the gel network. Moreover, using the MFIS method, a significant interaction between hydrogel and macromolecules was observed, in particular for A488 samples. The MTI results support the idea of the attractive interaction of Alexa-labelled particles and the gel, showing that the fluorescence intensity in the hydrogel was higher than that of the surrounding solution at the end of the measurements. This suggests to use uncharged dyes or, in case of charged dyes, to add a sufficiently high salt concentration for future investigations.

The heterogeneity inside a single hydrogel sample was probed on a length scale of 10  $\mu\text{m}$  in anisotropy experiments by comparing different pixels and hence different positions in the hydrogel (Fig. 2). Furthermore, for the experiments at pH 10, the scattering of data from various independent samples in Fig. 12b was significantly beyond shot noise limits (or other experimental uncertainties), revealing a heterogeneity, which persisted over the complete measurement times.<sup>82,83</sup>

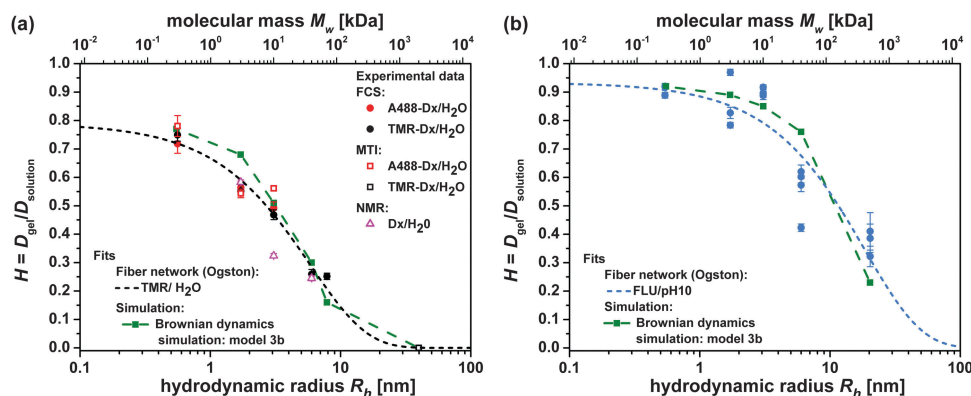


**Fig. 12** Hindrance factors  $H = D_{\text{gel}}/D_{\text{sol}}$  of dextrans in hydrogel. A488 (red), TMR (black) and unlabelled samples (magenta) measured in deionized water (a), FLU labelled samples (blue) measured in 20 mM potassium carbonate buffer at pH 10 (b). Experimental data: FCS (filled circles); MTI (open squares); NMR (open triangles); fitted model function: fiber network (eqn (18), dashed black and blue lines, parameters Table 6) and Brownian dynamics simulation (green points). The errors are the standard errors of repeat measurements.

Despite our application of a wide range of methods and the general consistency of the results we have obtained, open questions remain. For example, while the hindrance factor in the limit of small tracer particle sizes tends to 1 in our FLU/pH 10 system, it seems to approach  $\sim 0.8$  in our TMR/H<sub>2</sub>O system (Fig. 12). A value close to 1 might still be approached for smaller tracer particles in our H<sub>2</sub>O system, but we could not investigate these in our study due to experimental limitations. If one assumes that there really is a difference for smaller tracer molecules, the question whether this is due to different swelling in different environments or caused by different interactions of the matrix with different dyes cannot be answered with certainty yet.

For future studies, the diffusion of the same dextran molecules with the same dyes in differently crosslinked matrices should be explored systematically in order to distinguish between different modes governing the translocation.

## Abbreviations

|  |                               |
|--|-------------------------------|
| Mass concentration of polymeric material in total volume                                 | [T]                           |
| Weight fraction of cross-linker with respect to the total mass of the polymeric material | $C_R$                         |
| Diffusion time   | $t_d$                         |
| Gel disk radius  | $R_d$                         |
| Volume dry polymer   | $V_p$                         |
| Volume gel after swelling  | $V_{\text{gel}}$              |
| Mass   | $m$                           |
| Water density  | $\rho_{\text{H}_2\text{O}}$   |
| Polymer density  | $\rho_p$                      |
| Polymer volume fraction in the swollen state   | $\varphi$                     |
| Molecular weight of the polymer between cross-links points                               | $M_c$                         |
| Molecular weight of the repeating units  | $M_r$                         |
| Polymer mesh size  | $\xi$                         |
| Cross-linking degree in the hydrogel   | $X$                           |
| Carbon-carbon bond length  | $\zeta$                       |
| Flory characteristic ratio   | $C_n$                         |
| Numerical aperture   | NA                            |
| Detection volume in MFIS   | $V_{\text{det}}$              |
| Temperature  | $T$                           |
| Diffusion coefficient  | $D$                           |
| Gradient pulse width   | $\delta$                      |
| Diffusion delay  | $\Delta_N$                    |
| FCS fit model function   | $G(t_c)$                      |
| Triplet time   | $t_T$                         |
| Triplet amplitude  | $A_T$                         |
| Correlation time   | $t_c$                         |
| Confocal volume radius in $x$ and $y$  | $\omega_0$                    |
| Confocal volume radius in $z$  | $z_0$                         |
| Detection probability  | $w(x,y,z)$                    |
| Number of molecules  | $N$                           |
| Molecular fraction   | $x_i$                         |
| Position coordinates   | $x, y, z$                     |
| Fluorescence intensity   | $F, F_{\parallel}, F_{\perp}$ |

|   |                   |
|---|-------------------|
| Polarization correction factors                         | $l_1, l_2$        |
| Fluorescence anisotropy of species $i$                  | $r_i$             |
| $G$ -Factor   | $G$               |
| Intensity fit parameters in MTI                         | $P, p, Q, q$      |
| Echo intensities  | $E_i, E_0$        |
| Gyromagnetic ratio                                      | $\gamma$          |
| Gradient amplitude at increment $i$                     | $g_i$             |
| Delay between pulses                                    | $\tau_N$          |
| Boltzmann constant                                      | $k_B$             |
| Lattice constant  | $a$               |
| Distance in simulations models                          | $s_{ij}$          |
| Radius  | $R$               |
| Hydrodynamic radius                                     | $R_h$             |
| Matrix particle radius                                  | $R_{\text{obst}}$ |
| Position of particles in simulations models             | $\vec{s}$         |
| Mean square displacement                                | $\Delta s^2$      |
| Time, reference time                                    | $t, t_0$          |
| Potential between $i$ and $j$ particles                 | $U_{ij}$          |
| Energy steric constant                                  | $\varepsilon_s$   |
| Energy Gaussian constant                                | $\varepsilon_G$   |
| Energy attractive constant                              | $\varepsilon_a$   |
| Constant in simulations models                          | $b$               |
| Additive diameter                                       | $\sigma_{ij}$     |
| Position of minimum in simulations models               | $l_{ij}$          |
| Hindrance factor  | $H$               |
| Charge  | $Z_i$             |
| Effective binding constant                              | $K_d'$            |
| Ionic strength  | $I$               |
| Effective ion radius                                    | $R_i$             |
| Activity  | $a_i$             |
| Concentration   | $c_i$             |
| Activity coefficient                                    | $f_i$             |
| Debye-Hückel constants                                  | $A, B$            |
| Debye length  | $\kappa^{-1}$     |
| Photon number   | $N_F$             |
| Fluorescence lifetime of species $i$                    | $\tau_i$          |
| Radiative lifetime of species $i$                       | $\tau_{r,i}$      |
| Bessel function   | $I_0$             |
| Radial position inside an infinity cylinder for MTI fit | $s, s'$           |
| Fiber radius  | $R_f$             |

## Acknowledgements

C. J., H. L., S. U. E., and C. A. M. S. gratefully acknowledge partial financial support from the Strategic Research Fund of the HHU. Additional funding was given to D. W. by BioSoft and to C. E. S. and H. L. by the ERC Advanced Grant INTERCOCOS (grant agreement 267499).

## References

- 1 S. T. Balke, A. E. Hamielec, B. P. LeClair and S. L. Pearce, *Ind. Eng. Chem. Prod. Res. Dev.*, 1969, **8**, 54–57.
- 2 F. Chen, P. Tillberg and E. Boyden, *Science*, 2015, **347**, 543–548.

- 3 V. E. Barsky, A. M. Kolchinsky, Y. P. Lysov and A. D. Mirzabekov, *Mol. Biol.*, 2002, **36**, 437–455.
- 4 T.-O. Peulen and K. J. Wilkinson, *Environ. Sci. Technol.*, 2011, **45**, 3367–3373.
- 5 S. Brahim, D. Narinesingh and A. Guiseppi-Elie, *Biomacromolecules*, 2003, **4**, 1224–1231.
- 6 N. Murthy, Y. X. Thng, S. Schuck, M. C. Xu and J. M. J. Fréchet, *J. Am. Chem. Soc.*, 2002, **124**, 12398–12399.
- 7 P. Gupta, K. Vermani and S. Garg, *Drug Discovery Today*, 2002, **7**, 569–579.
- 8 R. Morita, R. Honda and Y. Takahashi, *J. Controlled Release*, 2000, **68**, 115–120.
- 9 S. Sershen and J. West, *Adv. Drug Delivery Rev.*, 2002, **54**, 1225–1235.
- 10 D. T. Eddington and D. J. Beebe, *Adv. Drug Delivery Rev.*, 2004, **56**, 199–210.
- 11 O. Wichterle and D. Lim, *Nature*, 1960, **185**, 117–118.
- 12 H.-W. Kang, Y. Tabata and Y. Ikada, *Biomaterials*, 1999, **20**, 1339–1344.
- 13 A. S. Hoffman, *Adv. Drug Delivery Rev.*, 2002, **54**, 3–12.
- 14 A. Z. Abidin, T. Puspasari and W. A. Nugroho, *Procedia Chem.*, 2012, **4**, 11–16.
- 15 R. Zolfaghari, A. A. Katbab, J. Nabavizadeh, R. Y. Tabasi and M. H. Nejad, *J. Appl. Polym. Sci.*, 2006, **100**, 2096–2103.
- 16 A. Meller, *J. Phys.: Condens. Matter*, 2003, **15**, R581.
- 17 A. Milchev, *J. Phys.: Condens. Matter*, 2011, **23**, 103101.
- 18 R. Metzler and J. Klafter, *Phys. Rep.*, 2000, **339**, 1–77.
- 19 F. Höfling and T. Franosch, *Rep. Prog. Phys.*, 2013, **76**, 046602.
- 20 K. Mecke, *Acta Phys. Pol., B*, 1997, **28**, 1747–1782.
- 21 A. Vagias, R. Raccis, K. Koynov, U. Jonas, H.-J. Butt, G. Fytas, P. Košován, O. Lenz and C. Holm, *Phys. Rev. Lett.*, 2013, **111**, 088301.
- 22 L. Haggerty, J. H. Sugarman and R. K. Prud'homme, *Polymer*, 1988, **29**, 1058–1063.
- 23 D. L. Holmes and N. C. Stellwagen, *Electrophoresis*, 1991, **12**, 253–263.
- 24 M. Kremer, E. Pothmann, T. Rössler, J. Baker, A. Yee, H. Blanch and J. M. Prausnitz, *Macromolecules*, 1994, **27**, 2965–2973.
- 25 J. Tong and J. L. Anderson, *Biophys. J.*, 1996, **70**, 1505–1513.
- 26 S. M. Russell and G. Carta, *Ind. Eng. Chem. Res.*, 2005, **44**, 8213–8217.
- 27 A. Stellwagen and N. C. Stellwagen, *Biopolymers*, 1990, **30**, 309–324.
- 28 J. S. Fawcett and C. J. O. R. Morris, *Sep. Sci.*, 1966, **1**, 9–26.
- 29 M. P. Tombs, *Anal. Biochem.*, 1965, **13**, 121–132.
- 30 N. C. Stellwagen, *Biochemistry*, 1983, **22**, 6186–6193.
- 31 D. L. Holmes and N. C. Stellwagen, *Electrophoresis*, 1991, **12**, 612–619.
- 32 R. Rüchel and M. D. Brager, *Anal. Biochem.*, 1975, **68**, 415–428.
- 33 L. M. Lira, K. A. Martins and S. I. C. D. Torresi, *Eur. Polym. J.*, 2009, **45**, 1232–1238.
- 34 Z. Blank and A. C. Reimschuessel, *J. Mater. Sci.*, 1974, **9**, 1815–1822.
- 35 A. G. Ogston, B. N. Preston and J. D. Wells, *Proc. R. Soc. London, Ser. A*, 1973, **333**, 297–316.
- 36 S. Schneider and P. Linse, *Macromolecules*, 2004, **37**, 3850–3856.
- 37 S. Edgecombe, S. Schneider and P. Linse, *Macromolecules*, 2004, **37**, 10089–10100.
- 38 S. Schneider and P. Linse, *J. Phys. Chem. B*, 2003, **107**, 8030–8040.
- 39 S. Schneider and P. Linse, *Eur. Phys. J. E: Soft Matter Biol. Phys.*, 2002, **8**, 457–460.
- 40 B. A. F. Mann, K. Kremer, O. Lenz and C. Holm, *Macromol. Theory Simul.*, 2011, **20**, 721–734.
- 41 B. A. Mann, C. Holm and K. Kremer, *J. Chem. Phys.*, 2005, **122**, 154903.
- 42 B. A. Mann, R. Everaers, C. Holm and K. Kremer, *EPL*, 2004, **67**, 786.
- 43 P. A. Netz and T. Dorfmueller, *J. Chem. Phys.*, 1997, **107**, 9221–9233.
- 44 H. Pei, S. Allison, B. M. H. Haynes and D. Augustin, *J. Phys. Chem. B*, 2009, **113**, 2564–2571.
- 45 L. Johansson and J. E. Löfroth, *J. Chem. Phys.*, 1993, **98**, 7471–7479.
- 46 P. Licinio and A. V. Teixeira, *Phys. Rev. E: Stat. Phys., Plasmas, Fluids, Relat. Interdiscip. Top.*, 1997, **56**, 631–634.
- 47 H. Zhou and S. B. Chen, *Phys. Rev. E: Stat., Nonlinear, Soft Matter Phys.*, 2009, **79**, 021801.
- 48 K. Kremer, *Comput. Mater. Sci.*, 1998, **10**, 168–174.
- 49 R. Messing, N. Frickel, L. Belkoura, R. Strey, H. Rahn, S. Odenbach and A. M. Schmidt, *Macromolecules*, 2011, **44**, 2990–2999.
- 50 D. A. Carr and N. A. Peppas, *Macromol. Biosci.*, 2009, **9**, 497–505.
- 51 F. Ganji, S. Vasheghani-Farahani and E. Vasheghani-Farahani, *Iran. Polym. J.*, 2010, **19**, 375–398.
- 52 H. Durchschlag and P. Zipper, in *Ultracentrifugation*, ed. M. D. Lechner, Steinkopff, 1994, ch. 3, vol. 94, pp. 20–39.
- 53 J. Jovanovic and B. Adnadjevic, *Polym. Bull.*, 2007, **58**, 243–252.
- 54 M. K. Krušić, M. Ilić and J. Filipović, *Polym. Bull.*, 2009, **63**, 197–211.
- 55 A. M. Lowman and N. A. Peppas, *Macromolecules*, 1997, **30**, 4959–4965.
- 56 A. Thakur, *Chem. Biochem. Eng. Q.*, 2011, **25**, 181.
- 57 S. Weidtkamp-Peters, S. Felekyan, A. Bleckmann, R. Simon, W. Becker, R. Kühnemuth and C. A. M. Seidel, *Photochem. Photobiol. Sci.*, 2009, **8**, 470–480.
- 58 Y. Stahl, S. Grabowski, A. Bleckmann, R. Kühnemuth, S. Weidtkamp-Peters, K. G. Pinto, G. K. Kirschner, J. B. Schmid, R. H. Wink, A. Hülsewede, S. Felekyan, C. A. M. Seidel and R. Simon, *Curr. Biol.*, 2013, **23**, 362–371.
- 59 D. Wagner, M. Börgardt, C. Grünzweig, E. Lehmann, T. J. J. Müller, S. U. Egelhaaf and H. E. Hermes, *Rev. Sci. Instrum.*, 2015, **86**, 093706.
- 60 M. Holz, S. R. Heil and A. Sacco, *Phys. Chem. Chem. Phys.*, 2000, **2**, 4740–4742.
- 61 A. L. van Geet, *Anal. Chem.*, 1970, **42**, 679–680.

- 62 D. H. Wu, A. D. Chen and C. S. Johnson, *J. Magn. Reson., Ser. A*, 1995, **115**, 260–264.
- 63 G. Wider, V. Dötsch and K. Wüthrich, *J. Magn. Reson., Ser. A*, 1994, **108**, 255–258.
- 64 V. Sklenar, M. Piotta, R. Leppik and V. Saudek, *J. Magn. Reson., Ser. A*, 1993, **102**, 241–245.
- 65 M. Piotta, V. Saudek and V. Sklenář, *J. Biomol. NMR*, 1992, **2**, 661–665.
- 66 P. Sengupta, K. Garai, J. Balaji, N. Periasamy and S. Maiti, *Biophys. J.*, 2003, **84**, 1977–1984.
- 67 P. O. Gendron, F. Avaltroni and K. J. Wilkinson, *J. Fluoresc.*, 2008, **18**, 1093–1101.
- 68 J. Enderlein, I. Gregor, D. Patra, T. Dertinger and U. B. Kaupp, *ChemPhysChem*, 2005, **6**, 2324–2336.
- 69 J. Enderlein, I. Gregor, D. Patra and J. Fitter, *Curr. Pharm. Biotechnol.*, 2004, **5**, 155–161.
- 70 M. Koshioka, K. Sasaki and H. Masuhara, *Appl. Spectrosc.*, 1995, **49**, 224–228.
- 71 N. B. Vicente, J. E. Diaz Zamboni, J. F. Adur, E. V. Paravani and V. H. Casco, *J. Phys.: Conf. Ser.*, 2007, **90**, 012068.
- 72 L. Hodgson, P. Nalbant, F. Shen and K. Hahn, *Methods Enzymol.*, 2006, **406**, 140–156.
- 73 D. Wagner, J. Burbach, C. Grünzweig, E. Lehmann, S. U. Egelhaaf and H. E. Hermes, unpublished work.
- 74 W. S. Price, *Concepts Magn. Reson.*, 1997, **9**, 299–336.
- 75 C. S. Johnson Jr., *Prog. Nucl. Magn. Reson. Spectrosc.*, 1999, **34**, 203–256.
- 76 F. J. Millero, R. Dexter and E. Hoff, *J. Chem. Eng. Data*, 1971, **16**, 85–87.
- 77 P. G. Bolhuis, A. A. Louis, J. P. Hansen and E. J. Meijer, *J. Chem. Phys.*, 2001, **114**, 4296–4311.
- 78 A. A. Louis, P. G. Bolhuis, E. J. Meijer and J. P. Hansen, *J. Chem. Phys.*, 2002, **117**, 1893–1907.
- 79 J. Dzubiella, A. Jusufi, C. N. Likos, C. von Ferber, H. Löwen, J. Stellbrink, J. Allgaier, D. Richter, A. B. Schofield, P. A. Smith, W. C. K. Poon and P. N. Pusey, *Phys. Rev. E: Stat., Nonlinear, Soft Matter Phys.*, 2001, **64**, 010401.
- 80 M. P. Allen and D. J. Tildesley, *Computer Simulation of Liquids*, Oxford Science Publications, Oxford University Press, 1989.
- 81 B. J. Alder, D. M. Gass and T. E. Wainwright, *J. Chem. Phys.*, 1970, **53**, 3813–3826.
- 82 M. Y. Kizilay and O. Okay, *Macromolecules*, 2003, **36**, 6856–6862.
- 83 A. M. Hecht, R. Duplessix and E. Geissler, *Macromolecules*, 1985, **18**, 2167–2173.
- 84 P. Debye and E. Hückel, *Phys. Z.*, 1923, **24**, 185–206.
- 85 F. Hofmeister, *Arch. Exp. Pathol. Pharmacol.*, 1888, **24**, 247–260.
- 86 K. D. Collins and M. W. Washabaugh, *Q. Rev. Biophys.*, 1985, **18**, 323–422.
- 87 C. Eggeling, PhD dissertation, Georg-August-Universität zu Göttingen, 1999.
- 88 J. Stejskal and J. Horská, *Makromol. Chem.*, 1982, **183**, 2527–2535.
- 89 D. Toptygin, *J. Fluoresc.*, 2003, **13**, 201–219.
- 90 Z. Zhang, E. Nadezhina and K. J. Wilkinson, *Antimicrob. Agents Chemother.*, 2011, **55**, 1075–1081.
- 91 A. W. Moore Jr. and J. W. Jorgenson, *Anal. Chem.*, 1993, **65**, 3550–3560.
- 92 Z. Petrášek and P. Schwille, *Biophys. J.*, 2008, **94**, 1437–1448.
- 93 E. P. Petrov, T. Ohrt, R. G. Winkler and P. Schwille, *Phys. Rev. Lett.*, 2006, **97**, 258101.
- 94 J. Crank, *The Mathematics of Diffusion*, Clarendon Press, Oxford, 2nd edn, 1975.
- 95 T. Kihara, J. Ito and J. Miyake, *PLoS One*, 2013, **8**, e82382.
- 96 S. Lehmann, S. Seiffert and W. Richtering, *J. Am. Chem. Soc.*, 2012, **134**, 15963–15969.
- 97 B. Amsden, *Macromolecules*, 1998, **31**, 8382–8395.
- 98 L. Masaro and X. X. Zhu, *Prog. Polym. Sci.*, 1999, **24**, 731–775.
- 99 B. A. Westrin, A. Axelsson and G. Zacchi, *J. Controlled Release*, 1994, **30**, 189–199.